INVESTIGATION OF LONG PERIOD OSCILLATIONS IN AN ENCLOSED HARBOR

Eric C. Cruz, Dr. Eng.
Research Engineer

Toshio Aono, Dr. Eng.
Chief

Numerical Analysis Laboratory
Technical Research Institute
Toa Corporation
1-3 Anzen-cho, Tsurumi-ku, Yokohama 230, Japan

ABSTRACT

Field measurements were conducted to verify and quantify the long period oscillations in Hiratsuka Harbor in Japan. Time series data of water surface displacements were synthesized and wave statistics of the surf beat component obtained. A nonlinear dispersive wave model was used to simulate the wave transformation around and within the harbor, using part of measured time series for the incident wave. The measured time series, frequency spectra and significant wave statistics of the long period components at the gauging stations were adequately simulated in the computation. Applications to the simulation of the wave field due to a critical wave for two harbor design scenarios are shown.

1. INTRODUCTION

While it is a requirement in the design of most harbors that seawalls and appurtenant structures be able to tolerate wave periods of more or less 10 seconds, many instances suggesting that this may not be sufficient have been reported. Among these are severe agitation in the harbor during high waves and damages and accidents from maritime operations and mooring facilities. These are often seen in harbors located in the nearshore zone (the region starting from the wave breaking point to where the waves swash). For example, it was reported that in one port in Kochi Prefecture, Japan, at the height of a typhoon, the water surface in the interior oscillated by several minutes and the water level moved up by as much as 2 to 3 meters from high water level (Sawaragi et al., 1982). Based on studies made up to now, it is widely thought that the long wave components of the order of one minute included in the attacking wave approach the so-called natural frequency of oscillation of the harbor and caused the observed phenomenon.

The existence of long waves in mild-slope beaches was first reported by Munk (1949) who coined the term 'surf beat' to describe components with period of about 2 minutes which were thought to be caused by variations in the height of the surf zone. Tucker (1950) reported observations of 1.5 minute long waves with heights that are proportional to those of the short

period sea. In this paper, the terms 'long period oscillations' and 'surf beats' will be used interchangeably. Long period oscillations can also occur in a harbor with a small basin area. This is usually the case for artificial harbors that are constructed entirely from a configuration of breakwaters, seawalls or mounds, but without the benefit of natural physical features that would otherwise decrease the proportion of the structures relative to the basin area. Another situation for the occurrence or excitation of these oscillations is when the harbor is either partially enclosed through a single opening that acts, for example, as a navigation entranceway. If the harbor configuration is ill-designed, multiple reflections from the harbor interior can lead to amplification of the otherwise small long period components of the incoming waves.

An example of such harbor is Hiratsuka Harbor in Kanagawa Prefecture, Japan. This harbor was constructed initially for berthing of commercial fishery vessels, but will later be used for docking of leisure boats. In addition to having a small basin area and a single entrance, the fact that it is located within the breaking zone is another reason why it can be susceptible to such long period oscillations. Because of plans to install mooring facilities inside the harbor, an investigation of the effects of these oscillations has been evaluated to be extremely important.

A number of theoretical analyses have been proposed to explain the generation mechanism of surf beats. Symonds et al. (1982) showed that these are generated by variation in the excess momentum flux caused by breaking waves, and that they are generated between the extreme seaward and shoreward positions of the breaking point. Schaeffer and Svendsen (1988) later improved this theory by including the effects of the so-called groupiness associated with waves of various frequencies, and demonstrated that surf beat generation can continue up to the surf zone. Roelvink et al. (1992) proposed a model to describe cross-shore low-frequency motions generated by shoaling and breaking of wave groups on a beach. These theories, however, are valid under the assumption that wave motion is two-dimensional and that surf beats, once generated, would propagate out into the sea. These are not the case inside an actual harbor located in the breaking zone, since the motion is clearly three-dimensional and long period oscillations can easily propagate back and forth between the reflective walls.

When a harbor is to be used for docking of ships, it is important to be able to calculate the magnitudes of ship motions due to long period oscillations. Sawaragi and Kubo (1982) developed a numerical method to predict the long period motions of moored ships in a rectangular basin, and discussed the effects of berth location on these. However, since waves are assumed infinitesimal, this method is not applicable when the waves approach breaking around the basin. At present, characteristics of attacking waves containing significant long period components and the response of harbors to these have not been elucidated. Moreover, a practical method of computation that has been established for ordinary sea waves (about 20 seconds or less) has not been similarly established for surf beats. Hence, in cases where it is important to accurately estimate the magnitude of these oscillations, a detailed field measurement is necessary. This is generally prohibitive in terms of time and cost.

In this paper, we report on the investigation carried out to measure these long period motions in Hiratsuka Harbor. The first part reports on the field investigation and on the synthesis of measured data. The second part reports on numerical computations of wave transformation and on simulations of both field measurements and the wave field induced by a design wave. This investigation is part of a study commissioned to investigate the occurrence of long period oscillations in the harbor, and to propose remedial measures against the same under various scenarios of harbor functions.

2. DESCRIPTION OF HIRATSUKA HARBOR

2.1 Location

Hiratsuka Harbor is located along Hiratsuka coast in Kanagawa Prefecture, Japan on the side of Pacific Ocean (**Figure. 1**). The coast is part of Sagami Bay which is between two other bays - Tokyo Bay and Suruga Bay. Sagami Bay is partially protected from direct wave attack emanating from Pacific Ocean by the offshore island Oshima. The harbor is near the mouth of Sagami River so it has the natural merit of having a high interior tranquility. On the other hand, its location relative to the river mouth has led to accretion of sediments, causing changes in river topography. This has been identified as the cause of the increasing difficulty in navigating fishery vessels and the loss of stable navigation channels. Based on sonar recordings of a hydrographic survey executed in February 1995 when the South Breakwater (the oblique breakwater) was still incomplete, the sea bottom configuration in the harbor vicinity is as shown in **Figure 2**. Following the increase of leisure boat traffic in the harbor itself, normal fishery operations have also been hampered. It was therefore necessary for the harbor administration to allocate spatial resources for fishery and recreational purposes.

2.2 Construction

Construction of the East Breakwater commenced in 1989 and ended in 1992. A two-layer steel plate construction technique was used. Due to the fact that the South Breakwater, which acts as the main defense against waves that directly approach the coast, is situated in the breaking zone, a different construction strategy was adopted and the second phase of construction started in 1993. This part has a total length of 285 meters with 195 meters situated in shallow region. At present, all exterior breakwaters as well as those separating the inner and outer bays have been constructed. When completed, it will have the form shown in **Figure 3**. The harbor encloses an area of about 62,800 square meters.

2.3 Wind and wave climate

The wind climate at the coast of Hiratsuka is summarized in **Figure 4**. As can be seen, its wind pattern is characterized by a predominance of the north and north-northeast winds within a year and these two directions constitute more than half of the recorded data. Meanwhile, winds from the south as well as south-southwest blow between April and September, or about half of the year.

Measurements at the Offshore Hiratsuka Station of the National Disaster Defense Science and Technology Center (NDDSTC) showed that within a year, more than half of the waves have a height of 0.40 meter to 0.60 meter, and that waves less than 1 meter constitute 85 percent of all waves. Waves exceeding 2 meters constitute roughly 4 percent and they are generated during the typhoon season between summer and autumn. Moreover, more than half have periods from 4 to 8 seconds and long period components characteristic of swells increase during the typhoon season. There is a tendency for the wave period to increase with wave height. As for wave direction, waves from the south are dominant during winter and for all other seasons, waves from the south-

southeast are actively generated. The harbor was designed for the following conditions: (1) Mean water level (MWL) = High water level (HWL) +1.50 meters = Low water level (LWL) +0.00 meter (2) Depth: 2.0 to 4.0 meters (3) Wave direction: south-southeast, wave height: 4.60 meters, wave period: 14.9 seconds.

3. FIELD MEASUREMENTS

In order to quantify the magnitude and other characteristics of long period oscillations in Hiratsuka Harbor, continuous field measurements were conducted. The field investigation included the setting-up of required apparatus at selected locations. Time series of water depths, velocity components and pressures were recorded. Pressure measurements were converted to water surface displacement (or elevation) data. These will be used to synthesize a standard frequency spectrum at the offshore location, which is needed in the design of the harbor itself. Water surface displacements will also be used as raw time series data for the numerical simulation of wave transformation.

3.1 Flowchart of investigation

Figure 5 shows a flowchart of the investigation process. It starts with the gathering of required data through field measurements at the existing condition of the harbor, that is, with an incomplete seawall and under the existing sea bottom configuration. The data is then used to obtain the characteristics of the long period components of the incident wave (at a location sufficiently removed from the harbor and at a deep region). Simultaneously, computation for the characteristics of the wave amplification factors in the harbor interior is done. Concurrent with the data-gathering stage is numerical simulation of the wave field based on mathematical models, with data for the incident wave obtained from the measured data. Simulation results are then compared with the observed time records and wave statistics at all stations. When this validity check is completed, forecasting of the wave field and other characteristics due to a design wave is carried out.

3.2 Measuring devices and siting

In the field observations, automatic gauges were installed at the bottom of the sea at designated locations. These gauges are self-recording types with internal memory and equipped with long-duration battery packs and are well-known in Japan for their robustness and ease of handling. **Figure 6** shows the disposition of the measuring devices. Station 1 is located offshore at a depth of about 20 meters and about 1200 meters offshore of the harbor entrance. Station 2 is near the harbor mouth, while Station 3 is in the outer bay of the harbor. It is important to site a station offshore from the mouth in order to avoid the effects of directional distribution of wave energies due to wave diffraction around the corner of the oblique breakwater. Three stations in the harbor interior are sited relative to the locations of the openings in the inner bay and the walls.

There are two types of wave gauges installed, namely, pressure type and ultrasonic type. Both gauges are equipped with an electromagnetic current meter that measures the two horizontal components of velocities in orthogonal directions. The absolute direction with respect to the north-

south direction (azimuth) is determined through an orientation meter attached to both gauge types. The difference of the gauges is that the ultrasonic type can additionally simultaneously measure the wave height. Pressure-type gauges are generally installed in shallow water while the ultrasonic gauges are normally installed in deep water up to a maximum of about 45 meters. The displacement of the water surface is indirectly measured by converting the pressure readings into displacements through a linear transfer function. Pressure readings are used to determine the water depth from MWL and by adding the height of the device at the measuring point, the total depth to the sea bottom can be obtained. **Figure 7** shows a photograph of the ultrasonic wave gauge as installed in the sea.

3.3 Measurement method

In order to measure the characteristics of the long period components, the recording duration is taken longer than usual field measurements involving significant wave periods of only about 5 to 20 seconds. Based on preliminary computations, the highest value of the natural frequency (defined as the frequency at which the water level will oscillate without external forcing) is about 420 seconds, which means a one-hour cycle will yield 3600/420 = 8.6 waves of the longest period. To obtain a sufficient number of the long period waves and, at the same time, adequately resolve the ordinary sea waves, the recording times and sampling intervals have been set as follows:

Recording times: 4 hours in one day (6 times/day × 60 days = 360 data)

Sampling intervals: Ultrasonic gauge (water elevation, velocities) 0.50 sec, (pressure) 1.0 sec;

Pressure gauge (pressure, velocities) 0.50 sec

3.4 Observation period

It is necessary to conduct measurements during a high wave season. **Figure 8** shows the wave height non-exceedance probability plotted against month, which has been synthesized from measurements at the Offshore Hiratsuka Station of NDDSTC between 1988 and 1995. Based on this, relatively tranquil condition can be expected in January and February and that there is almost constant probability of non-exceedance of 2.0-meter waves, except for August and September. However, since the appearance of high waves is more probable in spring (March to May), it is desirable to conduct measurements in this season. Moreover, considering that the sea bottom will change when dredging commences, it was recommended that measurement be conducted as early as possible. With these considerations, actual measurement was carried out over a two-month period from March 18 to May 18, 1997.

4. RESULTS AND SYNTHESIS OF FIELD MEASUREMENTS

Figure 9 shows the history of the significant and maximum wave heights, significant and maximum periods, and wave direction at Station 1 within the two-month observation period. The highest wave occurred on March 30, between 6 and 10 a.m. with a significant wave height of 2.62 meters and a period of 8.3 seconds. The wave with the longest period, on the other hand,

occurred on April 23, between 2 and 6 p.m. with a significant height of 1.57 meters. Both of these waves came almost directly from the south. It is only in March that the significant wave exceeded 2.50 meters while there were about 3 days in April when the significant period was longer than 10 seconds.

Samples of the measured time series of water surface displacements at Stations 1, 4 and 5 are shown in **Figure 10**. Only 30-minute portions of the entire four-hour time series are shown for clarity. The heavy curve corresponds to the long period oscillations extracted according to the method to be discussed below. The existence of long period oscillations is obvious especially for the interior points, Stations 4 and 5, although these are also observed for the other three in various amounts (Note that the ordinates at the plots are different). The apparent periods of these oscillations also vary for each location. Moreover, the proportion of the long period oscillations relative to the sea waves (the remainder of the ordinates after the long period oscillations have been subtracted) are higher for the interior points, which seem to suggest that some form of energy transfer could be taking place as the waves propagate into the harbor.

In order to see the distribution of wave energy across the .frequency range, a standard spectral analysis has been carried out. The resulting frequency spectra are shown in **Figure 11** (Note that a conventional triangular window has been applied to the raw periodogram to reduce the side effects of the application of the Fast Fourier Transform). The ordinate has units of wave energy divided by frequency. At Station 1, wave energy is concentrated in the high-frequency sea waves with a peak at about 0.12 Hz. Although not shown here, there is a gradual decrease of the energy of the sea waves accompanied by corresponding increase in low-frequency energy observed at Station 2 essentially due to wave shoaling as the depth decreases from 20 meters offshore to about 7 meters in front of the South Breakwater at the entrance. At Stations 4 and 6 which are in the inner bay, the high-frequency energy has decreased by more than an order of magnitude from its offshore value while the energy in the low frequencies has increased by roughly one order of magnitude.

The distribution of wave direction, which is defined here to be the direction of the depth-averaged velocity vector, for this sample at all stations is shown in **Figure 12.** Note from **Figure 4** that the wind blows, and hence the sea waves propagate, to the north and north-northeast directions through most of the year. This tallies with the plot at Station 1. The wave direction changes noticeably at Station 2 mainly due to wave refraction so that the wave front is approximately parallel to the South Breakwater near the tip. This direction changes inside the harbor. At Station 3, the wave direction is strongly east-west, and can be attributed to the presence of the detached breakwater demarcating the inner and outer bays. At Station 6, the waves are significantly north-south propagating mainly due to diffraction through the smaller opening at the west side. On the other hand, the directional scatter at Stations 4 and 5 is wide due to the existence of multi-reflection within the harbor. Even at these locations, however, it is possible to determine a dominant direction (called mean direction) along which the velocity vector is oriented most of the time.

To separate the long period oscillations from the sea waves, a standard filtering procedure has been applied to the time series shown. **Figure 13** shows the flowchart of this procedure. After the frequency spectra have been obtained through a standard Fourier transform, a cut-off frequency f_c is visually determined as the apparent frequency at which the low-frequency energy is at its minimum. The long period component is extracted by multiplying the raw spectra with a filter function, and the result is reverted to time series via an inverse Fourier transform. This

extracted time series is the long period oscillation depicted as the heavy curve in **Figure 10**. The filter function, which is a step with a triangular taper of width cf_c, is shown in **Figure 14**.

The extracted time series can then be used to synthesize the characteristics of the long period oscillations, such as the maximum wave, significant wave, mean wave, etc. When a suitable parameter has been chosen as a representative characteristic of these long period oscillations, both the quantification and synthesis of field measurements are deemed to have been completed. Time series of ten other critical cases in the two-month data have been processed and plotted similarly to **Figures 10** and **11**. They all indicate the existence of considerable long period oscillations in Hiratsuka Harbor. Syntheses of the time series for the wave statistics, to be reported in conjunction with simulation results, quantify these oscillations.

5. MATHEMATICAL MODEL OF WAVE EVOLUTION AROUND HIRATSUKA HARBOR

The second stage of this investigation is the numerical computation of surf beats. This is done by applying a mathematical model of wave transformation of ordinary sea waves, except that the incident wave train, which is the forcing function, is the measured time series of water elevations with or without long period oscillations. Because of the occurrence of wave breaking around the harbor, it is very important that the model is applicable to nonlinear waves. The first part of numerical computations is the simulation of field measurements which will allow us to validate the model. The second part is the forecasting of the wave field in the harbor induced by a design wave. These two parts will be separately treated in the next sections but a general description of their common mathematical basis is treated in this section.

5.1 Model Equations

The mathematical model used in this investigation is a subset of the equations originally developed to study wave transformation over porous beds (Cruz et al. 1997). For horizontally two-dimensional wave transformation over impermeable sea beds, they are written as

$$\eta_t + \nabla \cdot [(h + \eta)\mathbf{u}] = 0 \tag{1}$$

$$\mathbf{u}_t + \mathbf{u} \cdot \nabla \mathbf{u} + g\nabla \eta + \frac{h^2}{6}\nabla(\nabla \cdot \mathbf{u}_t) - \left(\frac{1}{2} + \gamma\right)h\nabla(h\nabla \cdot \mathbf{u}_t) - \gamma gh\nabla[\nabla \cdot (h\nabla \eta)]$$
$$+ F_B + F_S + F_W + f\mathbf{u} = 0 \tag{2}$$

where η is the water surface displacement from MWL, $\mathbf{u} \equiv (u, v)$ is the depth-averaged horizontal velocity vector, h the water depth from MWL, g the gravity acceleration, $\nabla \equiv (\partial/\partial x, \partial/\partial y)$ the gradient operator, γ the dispersivity-extension factor, (x, y) the horizontal coordinates, t the time, and f the boundary damping function (**Figure 15**). Subscripts t denote differentiation with time.

Equations (1) and (2) are, respectively, the continuity and momentum equations. When expressed in normalized variables, terms in these equations group according to various orders of two nondimensional parameters, namely, the wave nonlinearity index $\varepsilon \equiv a_o/h_o$ and the dispersivity index $\mu \equiv h_o/l_o$, where a_o, h_o, and l_o respectively denote a characteristic wave amplitude, water depth and wavelength. The continuity equation is exact to all orders of ε and μ while the momentum equation has a truncation error of the order of $O(\varepsilon\mu^2, \mu^4, \varepsilon^2\mu^2, \mu^6, ...)$. The equations incorporate the leading order of wave nonlinearity, a requisite in modelling wave phenomena occurring in shallow water. Although only terms of order $O(\mu^2)$ are included in the momentum equation, the model with $\gamma = 1/15$ is applicable to highly dispersive wave fields because the linear dispersion relation corresponding to these equations is of the order of $O(\mu^4)$. These equations are collectively referred to as the dispersivity-extended Boussinesq equations for impermeable beds.

In order to incorporate natural phenomena which have not been considered in deriving the model, the terms F_B, F_S and F_W have been added to the basic momentum equation. F_B represents the wave breaking dissipation, F_S models structure damping and F_W models bottom friction. F_W is modelled as

$$F_W = \frac{f_w |\mathbf{u}|}{2(h+\eta)} \mathbf{u} \tag{3}$$

where f_w is a nondimensional coefficient that depends on the bottom material but is usually in the range 0.001 to 0.05. The absolute value in $\mathbf{u}$, which stands for the velocity magnitude, ascertains that the friction resistance is always opposite to the direction of fluid acceleration. The term F_S represents damping at structure discontinuities due to flow impedance and is formulated as a momentum exchange term

$$F_S = -\nabla \cdot (\sigma \nabla \mathbf{u}) \tag{4}$$

where σ is a flow-dependent momentum exchange coefficient. This is modelled semi-empirically as

$$\sigma = \alpha_M \sqrt{g} \left(h + \overline{\eta}\right)^{3/2} \tag{5}$$

where $\overline{\eta}$ is the mean water level. The coefficient α_M has a maximum value at a structure discontinuity and is zero elsewhere. Details and applications are found in Cruz and Aono (1997a).

5.2 Discretization of equations and time-marching procedure

Equations (1) and (2) are solved for the variables η and $\mathbf{u}$ for a known bathymetry and. structure configuration. Discretization is made using the finite-difference method. Spatial discretization is carried out on a staggered grid while time discretization is carried out using a

time-splitting method **(Figure 16)**. Reduction of the differential equations to their algebraic forms is done using the alternate-direction-implicit (ADI) concept. The algebraic equation for all spatial derivatives are centered-space while time derivatives are centered-time for the non-advection terms and linearly extrapolated (backward-time) for the advection terms. Special attention is given to the discretization of the nonlinear terms so that the entire solution scheme can have an accuracy of $O(\Delta x^2, \Delta t^2)$, where Δx and Δt are the grid size and time step, respectively. Solution starts from still water conditions and is marched into time with each step consisting of four stages in the following order: implicit solution for u^{n+1}, explicit solution for η^{n+1}, implicit solution for v^{n+2}, explicit solution for η^{n+2}. The ADI scheme is formulated such that the time marching of η and u can be done without the need for iterative solution within a time step, and hence reduce significantly the total time of simulation. This capability of the numerical scheme to produce a fast time-marching is very important in the simulation of irregular wave fields including considerable long wave components because wave field characteristics such as the significant wave height need to be synthesized from a long wave record in order for statistical variability to be small. For this particular investigation, this capability is even more important because the surf beat components have much longer periods than the ordinary sea waves and so require a much longer wave record.

5.3 Computation region and boundary conditions

Computation is carried out in a rectangular area which is conceptually divided into specific regions or zones **(Figure 17)**. In general, the rectangular area is chosen such that all sides can be treated as open boundaries. The interaction of the incident waves with the sea bottom, structures and boundaries produce various wave types that are appropriately treated only in specific regions. The central region, called the coexistence zone, is where all wave types - progressive, reflected and scattered waves - exist. The narrow outer region is assigned as a damping zone where only waves leaving the area, called outgoing waves, exist. A narrower strip between these two regions is assigned as the incidence zone where the incident wave train can be fed. Attachment of the damping region is a computational technique devised to enforce the open boundary condition, stating that open boundaries must freely allow the outgoing waves to propagate out of the computation region without causing artificial reflections into the interior. The properties of the damping function $f(x,y)$ in Equation (2), namely, its distribution, damping width and magnitude, can be theoretically determined such that this condition is satisfied for a given range of incoming wave frequencies (Cruz and Isobe, 1994). The damping distribution for the regions parallel to the y axis, for example, is

$$f = \xi \sqrt{\frac{g}{h}} \frac{N+1}{2F^N} x'^N \qquad (6)$$

where N is the order of distribution ($N=1$ for linear, $N=2$ for parabolic), F the damping width, ξ the damping coefficient and x' has its origin at the interior edge of the region. A two-dimensional distribution is shown later in this paper (**Figure 21**).

Interaction of waves with structures is enforced through a boundary condition relating the properties of the reflected waves to those of the incoming wave. This condition on must treat two physical realities: nonhomogeneity of structures and a range of incoming wave frequencies. Structures can be nonhomogeneous due to different reflectivities, material makeup and shape

along their length. The following boundary condition, which is suitable for the discretization of the model equations, has been obtained using a volume flux resolution method:

$$\left[u(h + \eta)\right]_{x,y}^{t+\Delta t} = \left|F_{xx}\right| \left[u(h + \eta)\right]_{x-\Delta x, y}^{t+\Delta t - \tau} \tag{7}$$

$$F_{xx} = \frac{1 - r}{\left\{1 + r^2 - 2r\cos(2k\Delta x\cos\theta)\right\}^{1/2}} \tag{8}$$

$$\tan\omega\,\tau = \frac{1 + r}{1 - r}\tan(k\Delta x\cos\theta) \tag{9}$$

where r is the reflection coefficient, $k = 2\pi/L$ the incoming wave number (L is the wavelength), $\omega = 2\pi f$ the angular frequency (f is the frequency) and θ the incoming wave direction. Equation (7) relates the velocity at a structure grid point at the current time level to the velocity at the adjacent non-structure grid point at an earlier time with a time lag τ which is computed from Equation (9). This condition is applicable to structures which are parallel or perpendicular to the coordinate axes, but a general condition for structures of arbitrary orientation is derived and applied in Cruz and Aono (1997b).

5.4 Wave breaking model

The effects of waves breaking are incorporated into the model through the breaking dissipation term F_B in the momentum equations. The functional form of the model of Watanabe and Dibajnia (1988), which is based on the linear wave theory and a friction type of dissipation, is modified here to take into account the finite amplitude of the waves:

$$F_B = -f_D \nabla^2 \mathbf{u} \tag{10}$$

The dissipation coefficient f_D is a linear function of its maximum value

$$f_{D\max} = \alpha_D g^{3/2} \frac{s(h + \eta)}{\omega^2} \sqrt{\frac{|\mathbf{u}| - u_r}{h(u_s - u_r)}} \tag{11}$$

where $\alpha_D = 2.50$, s is the equivalent bottom slope, u_r is the velocity of recovered waves, u_s is the velocity on a plane slope, and $|\mathbf{u}|$ is the amplitude of the velocity at the point of interest. The parameters u_r and u_s have been determined empirically as

$$u_r = 0.135C \tag{12}$$

$$u_s = 0.40(0.57 + 5.3s)C \tag{13}$$

The equivalent bottom slope s is taken along the direction of the instantaneous velocity vector $\mathbf{u}$:

$$s = \nabla h \cdot \mathbf{e_u} \equiv \frac{\partial h}{\partial x}\cos\theta_\mathbf{u} + \frac{\partial h}{\partial y}\sin\theta_\mathbf{u} \tag{14}$$

$$\theta_\mathbf{u} = \tan^{-1}\frac{v}{u} \quad 0 \le \theta_\mathbf{u} \le 2\pi \tag{15}$$

The wave celerity C is computed from its definition $C \equiv \omega/k$, and the dependence of the wave number and angular frequency at a given depth is obtained from the linear dispersion relation of Equations.(1) and (2):

$$\frac{\omega^2 h}{g} = \frac{k^2 h^2 (1+\gamma k^2 h^2)}{1+(1/3+\gamma k^2 h^2)} \tag{16}$$

The wavelength to be used in the determination of the wave-number depends on the direction of the propagation of the wave crest as follows:

$$L = L_x \cos\theta_\mathbf{u} \tag{17}$$

where L_x is the local wavelength along the coordinate axis. The above parameters are illustrated in **Figure 19**. At all time levels, the wave profile along an axis is broken down into individual waves using the zero down-crossing method. The crests within these individual waves are identified and a breaking criterion is applied to judge if these are breaking. Breakers have nonzero values of f_{Dmax} if the numerator in the radical of Equation (11) is positive. The breaking dissipation f_D is then linearly distributed between these maximum values. The breaking criterion of Isobe (1987), formulated in terms of the relative depth h/L_0 and bottom slope s, is used here:

$$\eta_b = 0.80\zeta_b h_b \tag{18}$$

$$\zeta_b = 0.53 - 0.30\exp\left(-3\sqrt{\frac{h_b}{L_0}}\right) + 5s^{3/2}\exp\left[-45\left(\sqrt{\frac{h_b}{L_0}} - 0.1)\right)^2\right] \tag{19}$$

$$L_0 \equiv 2\pi\frac{g}{\omega^2} \tag{20}$$

where subscript b denotes values at the breaking point and L_0 is the deep water wavelength. A wave crest is adjudged to be breaking if its η is at least equal to Equation (18).

6. SIMULATION OF MEASURED LONG WAVE OSCILLATIONS

The mathematical model described in the preceding has been used to simulate selected cases of wave records from the field measurements at Hiratsuka Harbor. This part provides a general validity check for the ability of the wave model to simulate the long period oscillations that have been verified in field measurements.

6.1 Computational Conditions

The conditions of simulation are shown below:

Incident wave conditions:

    Frequency spectrum: synthesized from field data

    $r_1 = 0$ $r_2 = 0$ M = maximum number of frequencies in field data

Discretization:

    $\Delta x = \Delta y = 10$ m

    $\Delta t = T_{1/3,in}/100$

Model Parameters:

    $\gamma = 0.066667$

    $\alpha_M = 0.10$

    $f_w = 0.01$

Boundary damping:

    Offshore zone: $N = 1$, $F/h = 5$, $\xi = 0.50$

    Onshore zone: $N = 1$, $F/h = 5$, $\xi = 0.25$

    Lower side zone : $N = 1$, $F/h = 8$

    Upper side zone: $N = 1$, $F/h = 8$

Total length of computation: 60 minutes

Wave coexistence region: 800 m by 1500 m

Computation region: about 1050 m by 1720 m

Numerical simulation has been carried out by using the recorded time series of water surface displacements $\eta(t)$ at Station 1 as the incident wave train and computing the temporal

profiles at the locations of the five other stations. A view of the bathymetry around the harbor is shown in **Figure 20**. The sea bottom configuration was based on a combination of the data from the second hydrographic survey executed in December 1995 for the inner bay and those of the first one for the exterior and the existing harbor in February 1995 (see **Figure 2**).

The frequency spectrum is synthesized from the recorded time series according to the method to be described later. The effective frequency range spans the entire width of the spectrum. In general, the size of the grid is chosen so that a suitable compromise between computation time and accuracy is obtained. A larger grid size is desirable for speed of computation but a fine grid is required to resolve the shortest wave components that are of interest to the problem being investigated. Since long period oscillations are of primary interest, a relatively coarse grid of 10 meters is deemed appropriate for this model. The minimum time step required for stability of the numerical scheme is generally used and the size equal to the specified fraction of the incident significant period $T_{1/3,in}$ is affordably adequate to satisfy the stability requirement without sacrificing the resolvability of the ordinary sea wave components.

A small amount of dumping at structure discontinuities is prescribed based on the fact that armor blocks were presented around the tips of the South and West Breakwaters during the measurements. A nominal bottom friction is used. The properties of the boundary damping regions at each of four sides are prescribed using the simulation aid graphs for linear absorbers and irregular waves in Cruz and Isobe (1994) such that a maximum reflection of 3 percent into the interior is permitted. Note that since the width of the damping region is depends on depth, a smaller value of F/h is desirable offshore to minimize this extra region. The coefficients ξ need not be prescribed for the side damping zones since these are fixed by the other values and by a specified linear variation at their edges. The damping distribution in shown in **Figure 21**.

The length of the wave coexistence region is chosen to extend up to the deep water required by the location of Station 1, while the width is chosen so that the depth contour lines are more or less parallel to the shore. The area of the computation region depends on the width of the damping regions which, in turn, depends on the depth from MWL, and hence varies for each case of measurement.

Values of the reflection coefficient r have been assigned as shown in **Figure 22**. The outside faces of the South, West and East Breakwaters are protected with armor blocks throughout their lengths while their inside faces are quay walls which dissipate part of the incident wave energy. The Interior Breakwater, seawall and part of the West Breakwater have their exterior faces equipped with energy-dissipating features so that a lower reflectivity is suitable there. On the unfinished leg of the seawall and on the small berth at the corner, the lowest reflectivity has been assigned. It is well known that the reflection coefficient from a vertical wall also depends on the incoming wave frequency, with a larger value for smaller frequencies, that is, long waves tend to reflect a higher fraction of the incoming wave height. An empirical relation has been established for the armor blocks for this variation of r with frequency. It is also known that r varies with the incoming wave direction such that waves which are normal to the wall reflect more strongly and with symmetric deflection with the incoming wave, while those with a small cruising angle tend to be deflected asymmetrically. These known dependencies of r on frequency and direction have been altogether neglected in the present investigation and the values shown are meant more to distinguish between the relative reflectivities of the various parts of the breakwaters.

6.2 Cases of Simulation

The measured $\eta(t)$ at Station 1 have been synthesized and the maximum and significant wave heights and their corresponding periods for each 4-hour interval in the entire two-month record are shown in **Figure 9**. From this, the three cases tabulated in Table 1 have been selected for simulation. Case A is for the highest significant wave height of 2.62 m, Case B is for the longest significant wave period of 13.2 s, and Case C represents a nominal wave. The depth from mean water level for each has been determined by adding the tide level to the measured depths. The incident wave in these cases is generally north-bound or virtually normal to the shore.

Table 1
Wave conditions for simulation of field measurements

Case	A	B	C
Year/Month/Day/Hour	97.03.30.06	97.04.23.14	97.05.09.06
Reference Depth (SWL)	19.26 m	19.26 m	19.26
Depth (MWL)	20.47 m	19.96 m	20.59 m
$H_{1/3,in}$	2.62 m	1.57 m	1.90 m
$T_{1/3,in}$	8.3 s	13.2 s	8.50 m
Wave direction	S 174°	S 172°	S 174°

The raw time series at Station 1 can be used directly as the incident wave in the simulations. However, because the time step of the computation (0.083 s for Case A) is much smaller than the 0.50-sec sampling interval of the measurements, requiring interpolation for many of the time levels, and because a long simulation time extending beyond the 60-minute duration may be necessary for the longer wave period, a synthetic form of incident wave has been used instead of the observed time series. This synthetic wave $\eta_S(t)$ can be expressed as the Fourier series of the observed time series $\eta_0(t)$ (Tuah and Hudspeth, 1982) in the following way:

$$\eta_S(x,t) = \sum_{m=1}^{N/2} a_m \cos(k_m x - 2\pi f_m t - \varphi_m) \tag{21}$$

where m is the frequency component index, a the amplitude, $f = \omega/2\pi$ the frequency, φ the phase, and N the number of data. The amplitude and phase are computed from the Fourier coefficients as follows:

$$a_m = \sqrt{a_{sm}^2 + a_{cm}^2} \tag{22}$$

$$\varphi_m = \tan^{-1}\frac{a_{sm}}{a_{cm}} \qquad 0 \le \varphi_m \le 2\pi \tag{23}$$

$$a_{sm} = \frac{2}{N_2}\sum_{i=1}^{N_2}\eta_0(i\Delta t)\sin\left(2\pi\frac{im}{N_2}\right) \qquad m = 0,1,2,...\frac{N}{2} \tag{24}$$

$$a_{cm} = \frac{2}{N_2}\sum_{i=1}^{N_2}\eta_0(i\Delta t)\cos\left(2\pi\frac{im}{N_2}\right) \qquad m = 1,2,...\frac{N}{2}-1 \tag{25}$$

The raw time series is padded with zeroes at its end and the Fast Fourier Transform (FFT) is used to obtain the coefficients using a data count N_2 which is a power of 2:

$$N_2 = 2^{N_0} \qquad N_0 = \text{int}\left(\frac{\log N}{\log 2}\right)+1 \tag{26}$$

The wave number and frequency are related at a given depth through the dispersion relation

$$4\pi^2 f_m^2 = gk_m \tanh k_m h \tag{27}$$

Specification of the horizontal velocities is also required by the simulation. From linear wave theory of monochromatic waves, the depth-integrated velocity is proportional to wave celerity C as follows:

$$u = \frac{\eta}{h}C \tag{28}$$

so that the synthetic velocity time series for the irregular waves can be expressed as

$$u_S(x,t) = \frac{2\pi}{h}\sum_{m=1}^{N/2}\frac{f_m}{k_m}a_m\cos(k_m x - 2\pi f_m t - \varphi_m) \tag{29}$$

Equations (21) and (29) have been used to prescribed the incident wave time series at Station 1.

Figure 23 plots measures and simulated time series of η for Case A at the six stations over a 20 -minute time range (note that the ordinate scale varies among stations). As can be seen, long period oscillations are observed in the harbor interior and become particularly prominent in the inner bay. The period of these oscillations depends on the location, and it appears that it is shorter for stations near the entrances in the interior (Stations 3, 4 and 6). While it remains to be verified, this characteristic tends to be related to the pumping motion associated with oscillating enclosures with a narrow entrance. The sea waves that ride on top of these long period motions appear to be simulated with the correct order of magnitude, except at Stations 2 and 3.

A standard spectral analysis described in Section 4 has been performed for the simulated time series and the results are shown in **Figure 24** (note that both axes are plotted on a log scale). Based on the spectrum at Stations 1 and 2, the cut-off frequency is at around $f=0.05$ Hz, or a period of 20 seconds. Measurements at Station 1 indicate the existence of substantial surf beat energy, although this is very small relative to the energy of the high-frequency sea waves. The growth of the surf beat is adequately predicted at Station 2, but it is underestimated at Stations 3 to 6. Moreover, the high-frequency wave components at Stations 3, 5 and 6 are overestimated and underestimated at Station 4. In spite of these differences, the general trend of energy distribution among these frequency ranges is adequately reflected by the simulation.

Figure 25 shows the time profiles $\eta(t)$ for Case B. Compared to Case A, where the incident wave is high while the period is nominal, the incident wave height for this case is nominal and the significant wave period is long. There is now a good agreement in the order of magnitudes of both the surf beat and sea wave components between the computation and measurements. The period of the surf beat at Station 5 appears to be shorter than in Case A while those at Stations 3, 4 and 6 appear to be smaller than that at Station 3. The corresponding frequency spectra are shown in **Figure 26**. The growth of the small surf beat component at Station 1 is well simulated at the harbor entrance, but the peak is underestimated at Stations 3 and 6. The high-frequency sea waves at Station 3 are overestimated as in Case A. Again, the proportion of long period wave energy to the high-frequency wave energy is generally simulated by the model.

6.3 Wave statistics of long period oscillations

Quantification of the long period oscillations has been through a conventional irregular wave analysis. Similar to what was done for the field data (see **Figure 13**), the surf beat component of the simulated time series is extracted using a cut-off frequency of 0.05 Hz. Then this surf beat time series is broken down into individual waves using the zero up-crossing (ZUC) method as shown in **Figure 27**. These waves are then sorted in decreasing order of wave height, defined as the difference in maximum and minimum η within 2 adjacent ZUC points. The average of the highest one-third of the waves (the significant wave) is denoted as $H_{1/3}$. The corresponding statistics of wave period is $T_{1/3}$.

Figure 28 shows the comparison between measured and computed values of $H_{1/3}$ of the long period oscillations for the three cases. $H_{1/3}$ of the sea wave components has also been plotted for comparison. (Note that the scales for Stations 3 to 6 are smaller than those for Stations 1 and 2). It can be seen that the computed $H_{1/3}$ agrees well with the measured values of the surf beat. There is an increase of magnitude of these oscillations from Station 1 to Station 2 which is essentially due to wave shoaling. As the waves enter the harbor, the magnitude decreases slightly due to a decrease of volume flux at the entrance. The ratio of the $H_{1/3}$ of the surf beat component to that of the ordinary sea waves generally increases as the waves propagate into the harbor. In particular this ratio appears to be highest at Station 4, where these two components have almost the same magnitude, while this is roughly 0.50 at Stations 5 and 6. This result of comparable magnitudes of the surf beat and sea wave components tallies with the observations by Wright et al. (1982) who also reported some cases where the surf beat energy exceeded that of the sea waves. Although citing observations on a plane beach, Guza and Thornton (1985) also reported that wave heights of surf beats and sea waves are about the same at the shoreline.

Figure 29 shows the comparison of the measured and computed values of the significant wave period $T_{1/3}$ of the long period oscillations and of the sea waves. $T_{1/3}$ of the measured surf beat component is roughly in the range 60 to 120 seconds inside the harbor, which is about 6 to 12 times the average $T_{1/3}$ at Station 1. Although $T_{1/3}$ of the sea waves in the interior is approximately constant as shown in **Figure 29** (b), $T_{1/3}$ of the surf beat decrease from Station 3 to Station 4 and increases at Stations 5 and 6. While $T_{1/3}$ of the surf beat measured at Station 1 in the 3 cases varies between 40 to 130 seconds, it is limited to the narrower ranges of 70 to 80 seconds in the outer bay and 55 to 120 seconds in the inner bay.

In the last figure, we notice that the computations generally overestimate $T_{1/3}$ of the surf beats in the harbor interior. The deviations are attributed to two reasons: (1) differences in water depths during the field measurements and those used in the computation, and (2) the effects of directional spreading. Table 2 shows the depths used for computation and those measured in the field. In the computation, the bathymetry in the harbor exterior was based on a hydrographic survey conducted when the South Breakwater was still incomplete (see **Figure 2**) and, although a second survey for the harbor interior bathymetry was conducted in December 1995, the time lag of at least 15 months between the field measurements and these surveys appears to have resulted in local but considerable depth alterations. In general, the harbor has become deeper at the inner bay and shallower at Station 2. Since surf beats have

Table 2
Comparison of water depths

Case	Sta 1	Sta 2	Sta 3	Sta 4	Sta 5	Sta 6
(A) 97.03.30.06						
Measurement	20.47	~5.65	5.17	4.30	5.25	6.12
Computation	20.47	7.69[a]	4.67[b]	3.31[b]	3.71[b]	3.89[b]
(B) 97.04.23.14						
Measurement	19.96	~6.79	7.20	2.61	3.65	4.56
Computation	19.96	7.18[a]	4.16[b]	2.80[b]	3.20[b]	3.38[b]
(C) 97.05.09.06						
Measurement	20.59	6.70	5.84	3.20	4.23	5.16
Computation	20.59	7.81[a]	4.79[b]	3.43[b]	3.83[b]	4.01[b]

a - Depth data based on hydrographic survey taken February 1995
b - Depth data based on hydrographic survey taken December 1995

long periods and behave as shallow water waves in the entire computation region, they tend to be more sensitive to depth compared to the ordinary sea waves. Although results are not shown here, a series of simple numerical experiments showed that modifying the depths around Stations 3 to 6 to match the measured depths for each case showed marked improvement of the agreement in $T_{1/3}$ while maintaining the good comparison in $H_{1/3}$. The other possible cause of deviations is the neglect of directional distribution of wave energy. Considering that the offshore islands (see **Figure 1**) can cause long waves that approach directly from the ocean to be scattered in all directions, a directional distribution of wave energy could be occurring at Station 1. Inclusion of this phenomenon in the computations would require measurement of directional spectra at Station 1, a task which is a lot more difficult to execute in the field.

In spite of the assumptions made, the ability of the model to predict the magnitude of the long period oscillations has been verified by these three cases, representing a high wave, a long wave and a nominal wave incident at Station 1. Several other simulations for cases intermediate between these three were also carried out, but the results do not provide additional information. It should be mentioned too that while a direct comparison of the time series is standard procedure for regular wave transformation or for simulation of irregular waves in laboratory experiments, such a method of comparison is unwarranted for the actual waves measured here since the phase relations in the field data can never be reproduced in a numerical simulation that commences from still water conditions. The alternative comparison is through the frequency spectra, and the results presented corroborate the conclusions already made.

7. NUMERICAL SIMULATION OF A DESIGN WAVE

The wave evolution model has been used to simulate the conditions induced by a design wave. In this case, artificial modification to the bathymetry in the harbor interior or breakwater configuration, or both, is studied as to how it would affect the wave regime in the interior. An immediate objective is the quantification of the critical wave condition in terms of the maximum wave heights induced by such design wave. This parameter is extremely important, for example, in the design of mooring facilities and seawall grading.

A design wave is determined based on a synthesized frequency spectrum of measured wave heights and a chosen return period. The wave heights are measured in deep water where shallow water effects can be neglected. A synthesis of the NDDSTC data gave the following critical wave at Station 1: $T = 14.2$ sec, $H_0 = 6.26$ meters, Direction: N + 187.5°. In order to carry out simulation on a finite region, the deep water wave height H_0 is converted to an equivalent height at a depth of 25.6 meters, which is the measured depth at the seawardmost station in the hydrographic surveys, using a sea bottom slope of 1/50. This yields a wave height $H=5.82$ meters.

7.1 Frequency spectrum parameters

A standard frequency spectrum (Goda, 1985) has been specified at the offshore location (**Figure 30**):

$$S(f) = 0.257 H_{1/3}^2 T_{1/3} (T_{1/3} f)^{-5} \exp[-1.03(T_{1/3} f)^{-4}] = af^{-5} \exp(-bf^{-4}) \tag{30}$$

$$a = 0.257 \frac{H_{1/3}^2}{T_{1/3}^4} \qquad b = \frac{1.03}{T_{1/3}^4} \tag{31}$$

The total wave energy E_T, equal to the area under the curve, is

$$E_T = \int_0^{\infty} S(f) df = \frac{a}{4b} \tag{32}$$

Considering that only a finite band of the spectrum can be used in numerical computations, it is necessary to define the following three parameters to delimit this band: (1) r_1 which is the fraction of low-frequency wave energy to be neglected (2) r_2 which is the fraction of high-frequency energy to be neglected, and (3) the number of frequency components M contained in the effective frequency band thereby defined. This band is delimited by the frequencies:

$$f_1 = \left[\frac{1.03}{\ln(1/r_1)} \right]^{1/4} \frac{1}{T_{1/3}} \tag{33}$$

$$f_2 = \left[\frac{1.03}{\ln[1/(1-r_2)]} \right]^{1/4} \frac{1}{T_{1/3}} \tag{34}$$

The amplitudes and frequencies contained in this band are determined based on a constant energy increment ΔE as follows:

$$\Delta E = \frac{1 - r_1 - r_2}{M - 1} E_T \tag{35}$$

$$f_m = \left\{ \frac{1.03}{\ln[r_1 + (m-1)\Delta E]} \right\}^{1/4} \frac{1}{T_{1/3}} \qquad m = 1, 2, \dots M \tag{36}$$

$$a_m = \sqrt{2\Delta E} \qquad m = 1, 2, \dots M \tag{37}$$

The time series for η and u_s are computed using Equations.(21) and (29) with the frequencies and amplitudes given by Equations.(36) and (37). However, unlike in the simulation of field measurements where the phases are part of the measured time series, the phases φ_m in this case have to be prescribed as random numbers between 0 and 2π.

Design wave simulations were obtained using the incident wave parameters below:

$H_{1/3,in}=5.82$ m $T_{1 3,in}=14.2$ s $h = 25.6+1.90$ m

$r_1 = 1 \times 10^{-3}$ $r_2 = 0.10$ $M = 96$

7.2 Wave field in nonpartitioned harbor induced by a design wave

The wave field in the existing configuration of the breakwaters has been simulated by prescribing an artificially modified interior bathymetry, shown in **Figure 31**. The inner bay is assumed dredged to maintain a uniform depth of 3 meters while the outer bay has an average depth of 3.5 meters and graduated to the existing sea bottom in the exterior. Based on a synthesis of long period oscillations from numerical simulations discussed in the previous section, a tide level of 1.90 meters was uniformly superimposed on the entire bathymetry. The seawall has $r=0.90$ now throughout its length.

Figure 32 shows a snapshot of various parameters of the wave field. The surface displacement shown in (a) indicates the extent of wave penetration in the interior and the effects of the breakwaters on the wave climate. A strong reflection of the incoming waves by the South Breakwater is seen, leading to the short-crested wave patterns in the left foreground. **Figure 32** (b) shows the wave breaking zones where the dissipation term f_D is nonzero, the size of the markers indicating its relative magnitude. There are two zones in which the breakers occur: (1) on the shallow side of the West Breakwater where the dissipation distribution is characteristic of dominantly progressive waves, and (2) in front of the South Breakwater, where the sea bottom is relatively deep but where the distribution is typical of partial standing waves due to oblique reflection from structures. Although the breakers do not penetrate the interior for this instance, there are few instances within the simulation period when they did penetrate. **Figure 32** (c) shows the horizontal velocity distribution (depth-averaged values) around the harbor. The exterior side of the West Breakwater has the velocity field of a progressive wave, the front of the South Breakwater has that of a reflection region while the interior has the confused, multi-directional velocity field typical of enclosed harbors. Note the extent to which the breakwaters protect the harbor from this high wave.

Figure 33 shows the contours of the maximum wave heights, normalized by H_{in} ($=H_{1/3,in}$), synthesized at the end of 60 minutes of simulation. Combined effects of refraction, reflection, diffraction and wave breaking have reduced the maximum wave to around 80% at the entrance. The maximum wave is within $0.40 H_{in}$ to $0.60 H_{in}$ in the outer bay and between $0.30 H_{in}$ and $0.45 H_{in}$ in the inner bay. It can be seen that generally, the higher waves occur near the breakwaters.

Figure 34 shows the distribution of significant waves in the interior. In contrast to the maximum wave height distribution, this shows a gradual distribution in the outer bay and an essentially constant one in the inner bay. These are characteristics of wave fields in enclosed harbors with reflective walls.

7.3 Wave field in partitioned inner bay due to a design wave

One of the alternative configurations contemplated in the final harbor is a partitioned inner bay. The actual partition is a vertical breakwater with slits that allow a degree of water movement between the resulting compartments. In the computation, this is modelled as a breakwater with a reflectivity of 0.90 on both faces. **Figure 35** shows the transient wave field due to the same design wave at the same instance as **Figure 32**. The breaking dissipation zones shown in (b) are almost similar to that of previous case indicating that the oscillations within the inner bay do not substantially affect the exterior. The velocity field shown in (c) in the inner bay, however, is significantly different from that of the previous case, so that the locations of the crests and troughs, shown by (a), are lagged from those in the nonpartitioned inner bay.

Figure 36 shows the maximum wave heights at the end of 60 minutes. It can be seen that, although the wave heights at the harbor entrance are essentially unchanged, those in the interior are redistributed. In general, the maximum heights in the East inner bay (adjacent to the East Breakwater) are increased by about $0.05H_{in}$ while those in the West inner bay and outer bays are decreased by roughly $0.05H_{in}$. **Figure 37** shows the corresponding significant wave heights. Although the values are almost the same with those for the previous case in the outer bay, the values in the West inner bay is smaller by roughly $0.05H_{in}$. From these results, it can be concluded that the wave field in the interior is induced by a combination of wave motion due to diffraction of incident wave in the outer bay and by induced flow. This flow is due partly to wave nonlinearity and partly due to currents generated by the broken wave. This combined motion is first brought into the East inner bay and recirculated within the interior bay through multi-reflection by the breakwaters, while a smaller portion is transported back into the outer bay through the smaller entrance in the West inner bay. The partition then hinders the circulating portion of this motion so that the East inner bay trapped most of the wave energy and, consequently, the portion that would have been otherwise carried into the West inner and outer bays was reduced. A drastic reduction of wave heights in the West bay is not realized, however, since the portion of the diffracting wave in the outer bay going into the West bay is now increased as a result of a higher surface gradient between the outer and West inner bays.

8. CONCLUSIONS

The following conclusions are drawn from this study:

(1) Field investigation of the wave field variables around the enclosed structure of Hiratsuka Harbor, is reported. The methods and techniques adopted in the field measurement and the synthesis of the field data are described.

(2) Continuous field measurements over two-month period around Hiratsuka Harbor revealed the existence of long period oscillations or surf beat. The significant height of these oscillations can be as much as 0.40 meter for a composite wave $H_{1/3}$ of 2.62 meters at a depth of about 20 meters. Surf beats grow in magnitude in shoaling depths and their energy within the harbor can be of the same order of magnitude as the sea waves. The ratio of significant wave heights of the sea waves to these oscillations decreases spatially from the harbor entrance to the interior.

(3) Surf beats outside Hiratsuka Harbor can have a significant period of 130 seconds for a composite wave $T_{1/3}$ of 13.2 seconds at a depth of 20 meters. While this period is proportional to the composite waves' $T_{1/3}$ outside and away from the breakwaters, it is essentially independent of the same within the harbor, indicating that multi-reflection in the interior tends to smooth out statistical variability of the surf beat period.

(4) A mathematical model of evolution of nonlinear dispersive waves is applied to simulate the transformation of irregular waves around the harbor. The model includes wave diffraction, refraction and shallow water transformation, and by incorporating the effects of wave breaking, bottom friction and damping by structures, it becomes capable of simulating field conditions in an actual harbor. The numerical implementation of the model is described, with due account of the requirements of open boundaries and arbitrary reflectivities of breakwaters.

(5) The synthesis of time series of the water surface displacements shows that the significant wave heights of the long period oscillations can be reproduced by the wave model. The general trend in the evolution of the measured surf beat statistics is simulated well by the model, although there is an overestimation of the surf beat period in the harbor interior due mainly to deviations in actual and assumed depths.

(6) The distribution of wave energy with frequency is adequately simulated by the computations. The relative decrease of the sea wave energy and the relative increase of energy of the long period oscillations spatially from offshore to the inner bay observed in the field investigations is reflected in the simulations.

(7) Application to the simulation of the wave field induced by a design wave is shown and it is demonstrated that critical variables inside the harbor, such as the maximum wave height, can be computed under various design scenarios.

REPERENCES

1. Cruz, E.C., Isobe, M. and Watanabe, A. (1997): Boussinesq equations for wave transformation on porous beds. Coastal Engineering, Vol 30, pp. 125-156.
2. Cruz, E.C. and Aono, T. (1997a): Nonlinear wave field induced by offshore shoals and vertical structures. In: Proceedings, 7th International Offshore and Polar Engineering Conference, ISOPE, Vol 3, pp. 791-797.
3. Cruz, E.C. and Aono, T. (1997b): Simulation of nonlinear wave field induced by partially reflective harbors. (To appear in:) Proceedings, Pacific Coasts and Ports '97, IPENZ.
4. Cruz, E.C. and Isobe, M. (1994): Numerical wave absorbers for short and long wave modelling. In: Proceedings, International Symposium on Waves - Physical and Numerical Modelling, University of British Columbia, Vol 2, pp. 992-1001.
5. Goda, Y. (1985): Random seas and design of maritime structures. University of Tokyo Press, 323 pp.
6. Guza, R. T. and Thornton, E.B. (1985): Observations of surf beat. Journal of Geophysical Research, Vol 90, C2, pp. 3161-3172.

7. Isobe, M. (1987): A parabolic equation model for transformation of irregular waves due to refraction, diffraction and breaking. Coastal Engineering in Japan, Vol 30, No.1, pp. 33-47.

8. Munk, W.H. (1949): Surf beats. Transactions, American Geophysical Union, Vol 30, pp. 849-854.

9. Roelvink, J.A., Petit, H.A. and Kostense, J.K. (1992): Verification of a one-dimensional surf beat model against laboratory data. In: Proceedings, 23rd International Conference on Coastal Engineering, ASCE, pp. 960-973.

10. Sawaragi, T., Kubo, M. and Aoki, S. (1982): Various problems related to sheltering in an ocean-connected fishery harbor. In: Proceedings, Coastal Engineering Conference, JSCE, Vol 29, pp. 516-519 (in Japanese).

11. Sawaragi, T. and Kubo, M. (1982): Long period motions of a moored ship induced by harbor oscillations. Coastal Engineering in Japan, Vol 25, pp. 261-275.

12. Schaeffer, H.A. and Svendsen, I.A. (1988): Surf beat generation on a mild-slope beach. In: Proceedings, 20th International Conference on Coastal Engineering, ASCE, pp. 1058-1072.

13. Symonds, G., Huntley, D.A. and Bowen, A.J. (1982): Two-dimensional surf beat: long wave generation by a time-varying break point. Journal of Geophysical Research, Vol 87, C1, pp. 492-498.

14. Tuah, H. and Hudspeth, R. (1982): Comparisons of numerical random sea simulations. Journal of Waterway, Port, Coastal and Ocean Engineering, ASCE, WW4, pp. 569-584.

15. Tucker, M.J. (1980): Surf beats: sea waves of 1 to 5 minute period. In: Proceedings, Royal Society of London, A202, pp. 565-573.

16. Watanabe, A. and M. Dibajnia (1988): A numerical model of wave deformation in surf zone. In: Proceedings, 20th International Conference in Coastal Engineering, ASCE, pp. 578-58.

17. Wright, L.D., Guza, R.T. and Short, A.D. (1982): Surf zone dynamics on a high energy dissipative beach. Marine Geology, Vol 45, pp. 41-62.
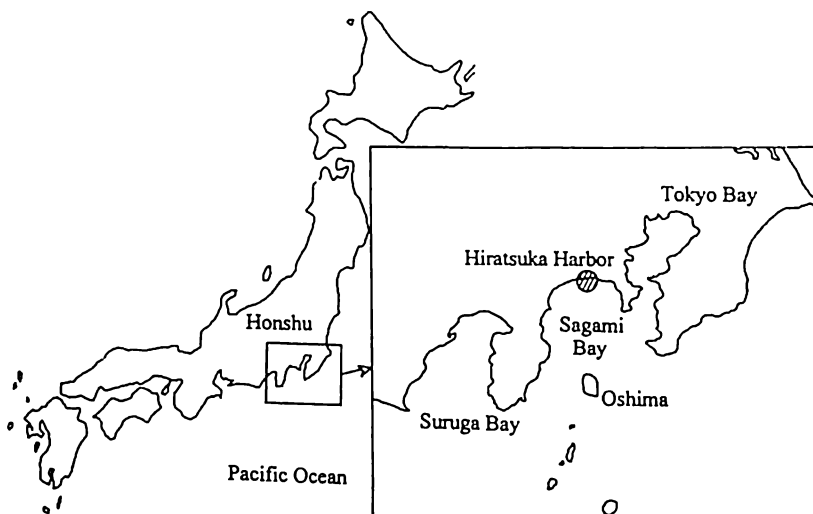
Figure 1. Location of Hiratsuka Harbor
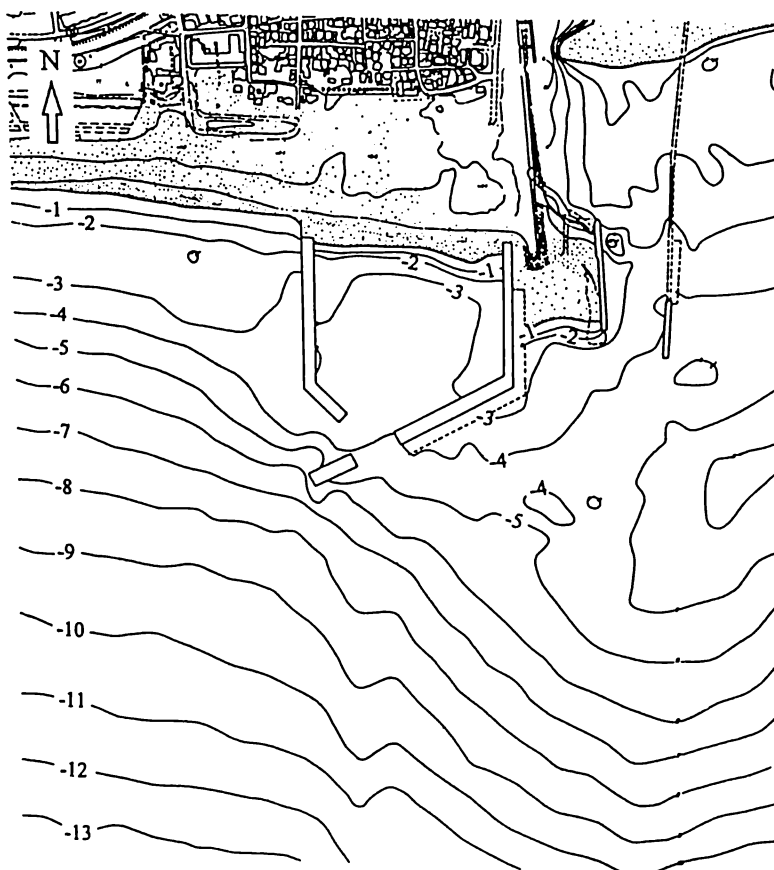
Figure 2. Vicinity and bathymetry of Hiratsuka Harbor (based on depth data taken February 1995)
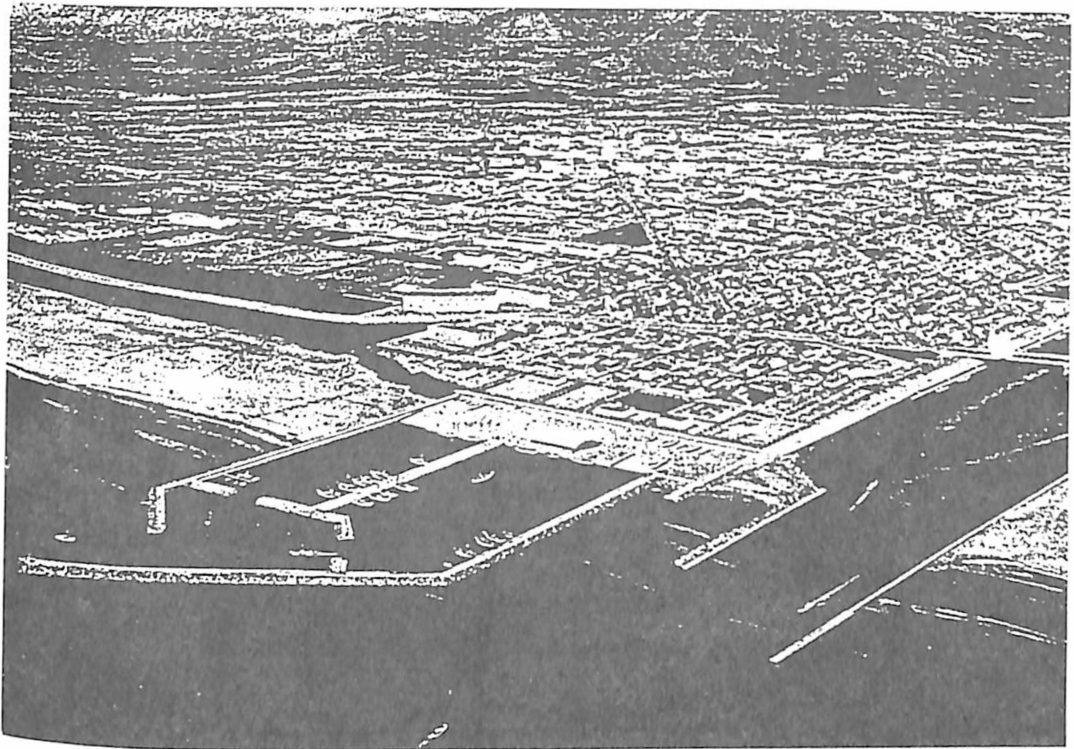
Figure 3. A perspective of the completed harbor

Average Wind (Offshore Hiratsuka)
Period: Oct 1986 - Sep 1991

Wind speed (m/s)

20.0-
15.0- 19.9
10.0- 14.9
5.0- 9.9
0.1- 4.9

Appearance Probability
Scale
0 10 20 30 40

Jan - Mar

Apr - Jun

Jul - Sep

Oct - Dec

Numbers in inner circle:
Upper - Percentage of calm (less than 0.1m/s) condition
Lower - Percentage of measurement
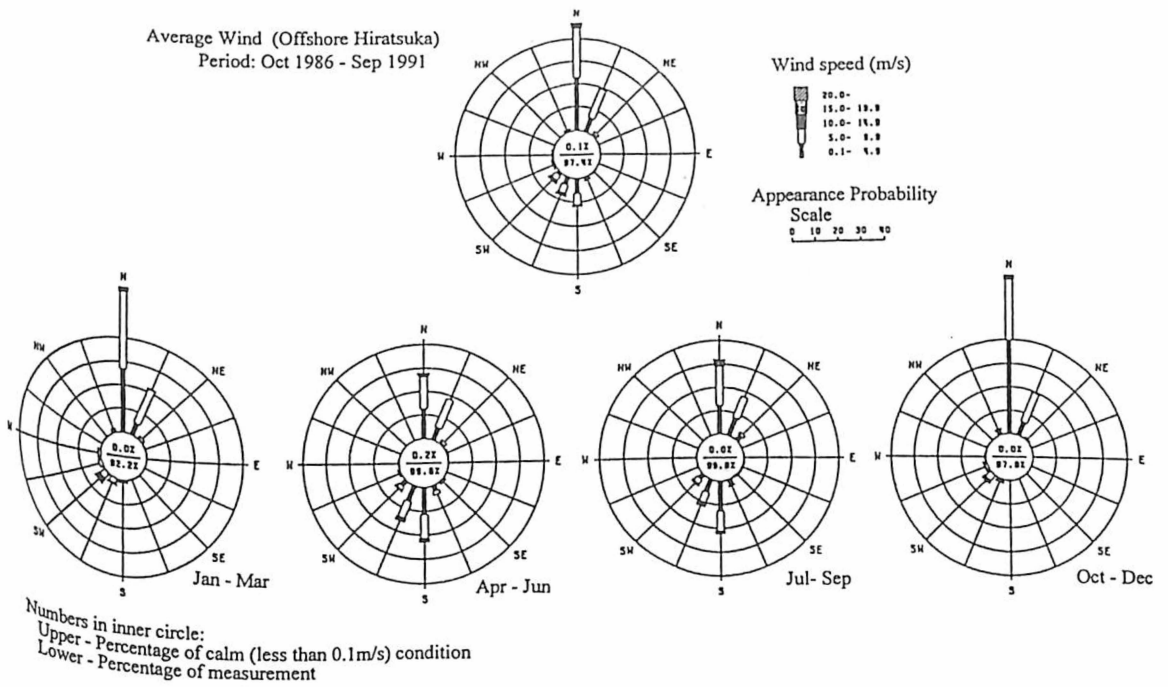
Figure 4. Distribution of wind speed and direction
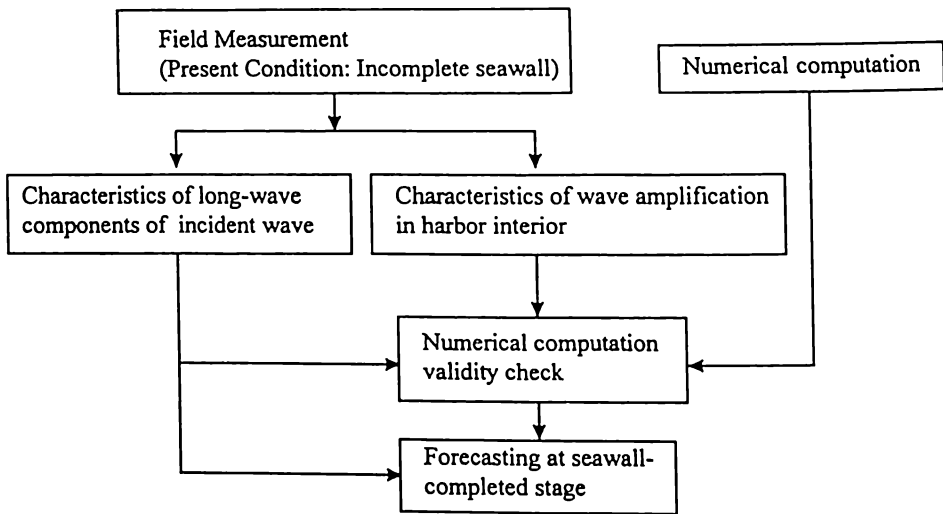
Figure 5. Flowchart of investigation
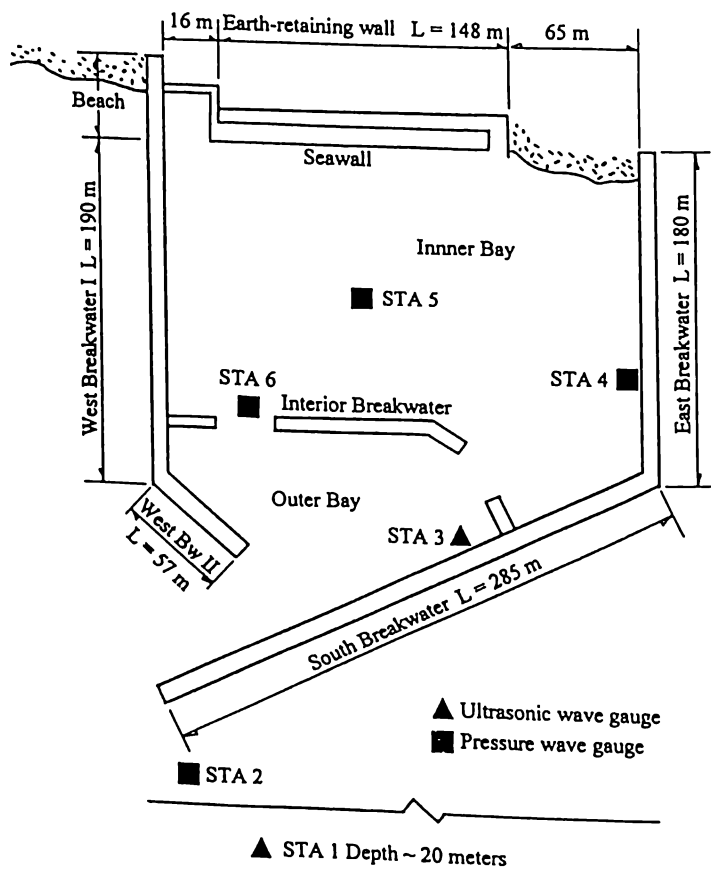
Figure 6. Layout of measuring devices
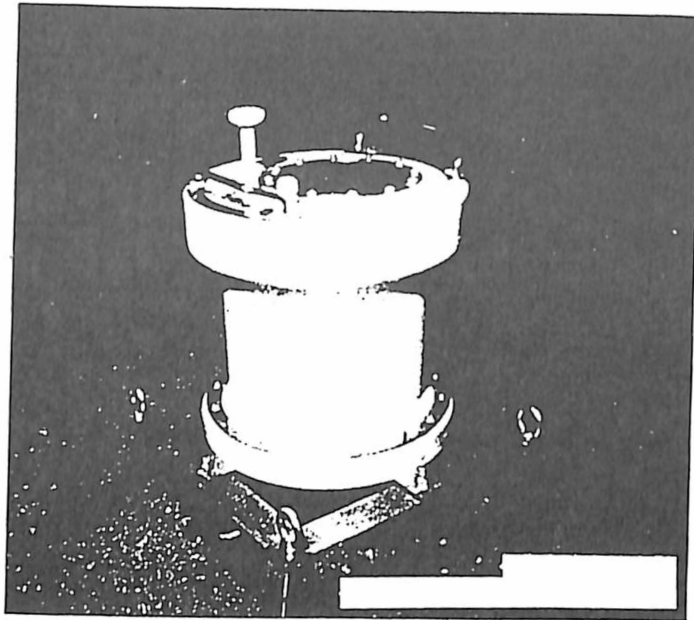
Figure 7. Ultrasonic wave gauge
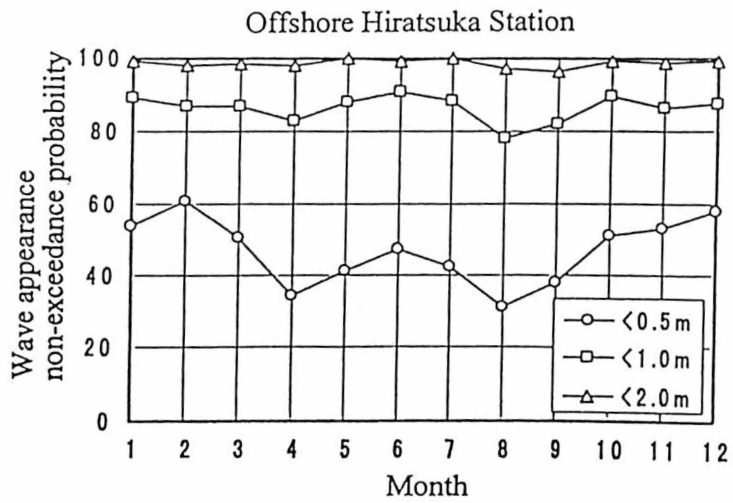
Figure 8. Wave height non-exceedance probability versus month
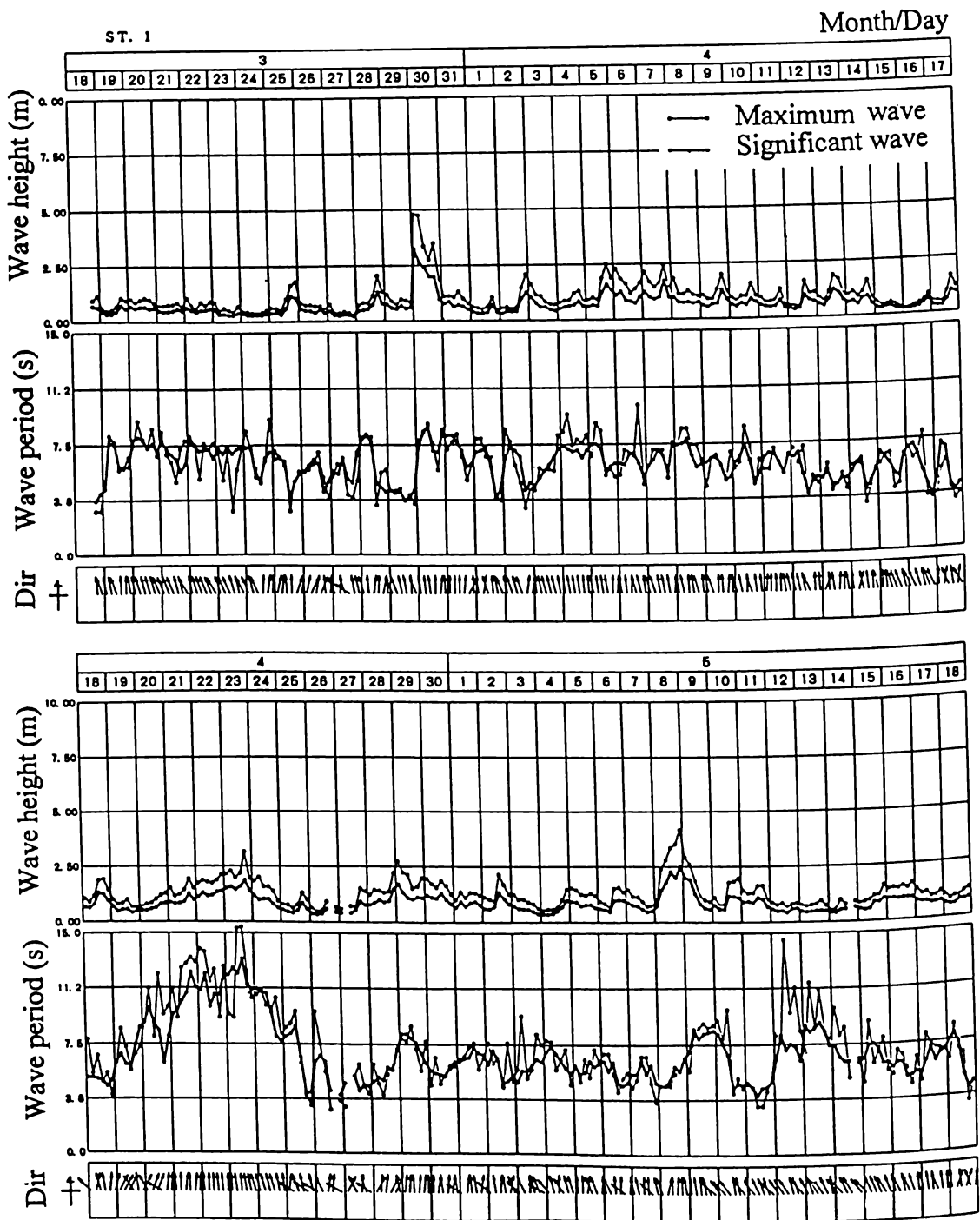
Figure 9. Measured wave heights, periods and direction at Station 1 (March 18 to May 18, 1997)

MEASURED
97.03.30.06   h=19.26 +1.21m   Sign.Wave: H=2.62m   T=8.3s
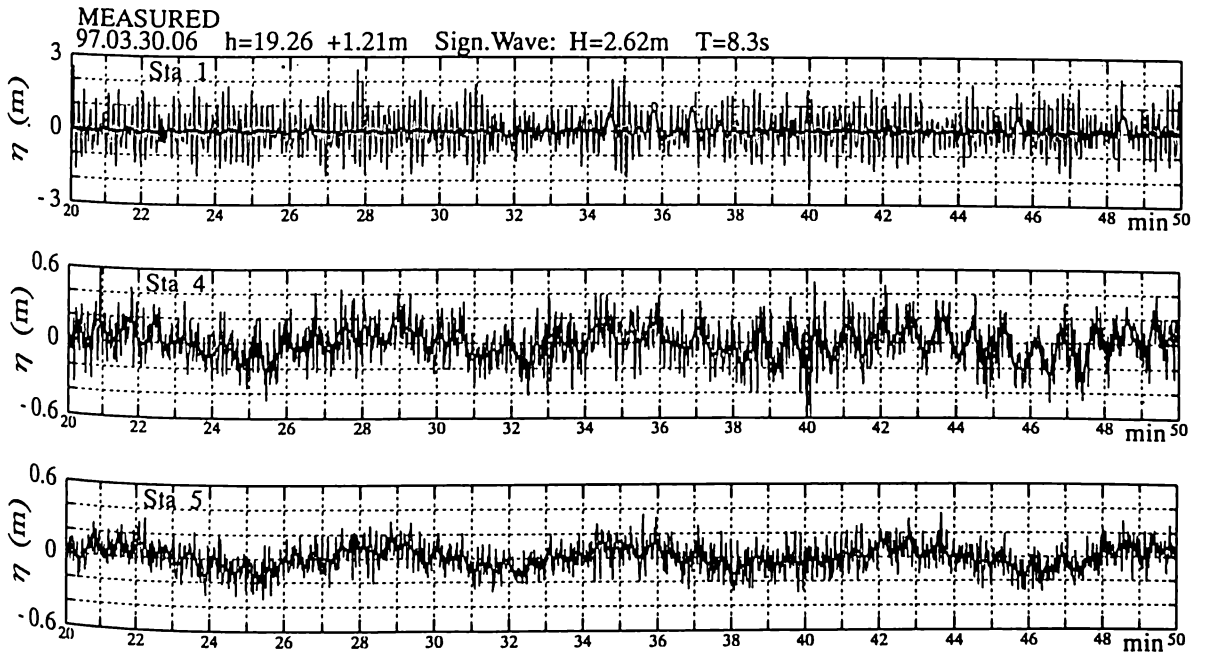
Figure 10. Time series of measured surface displacement at Stations 1, 4, 5 Case 97.03.30.06. The heavy curve is the long period oscillation extracted with $f_c = 0.05$ Hz
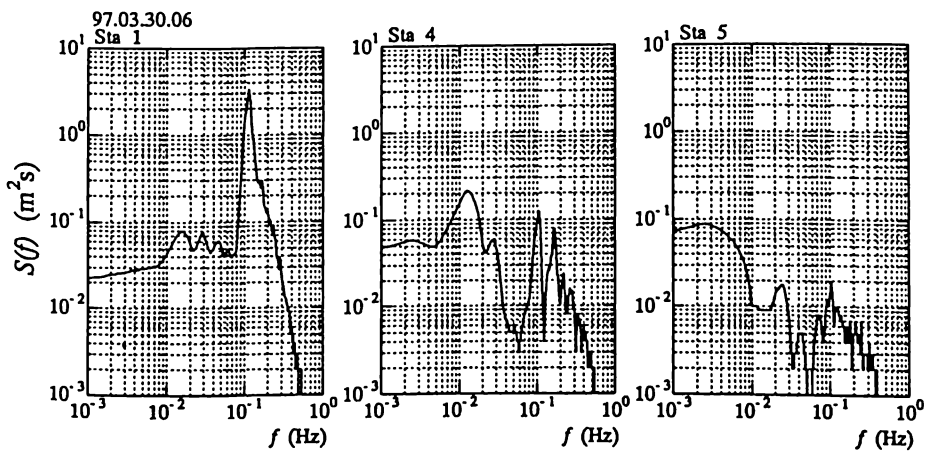
Figure 11. Frequency spectra of measured surface displacements at Stations 1, 4, 5 Case 97.03.30.06
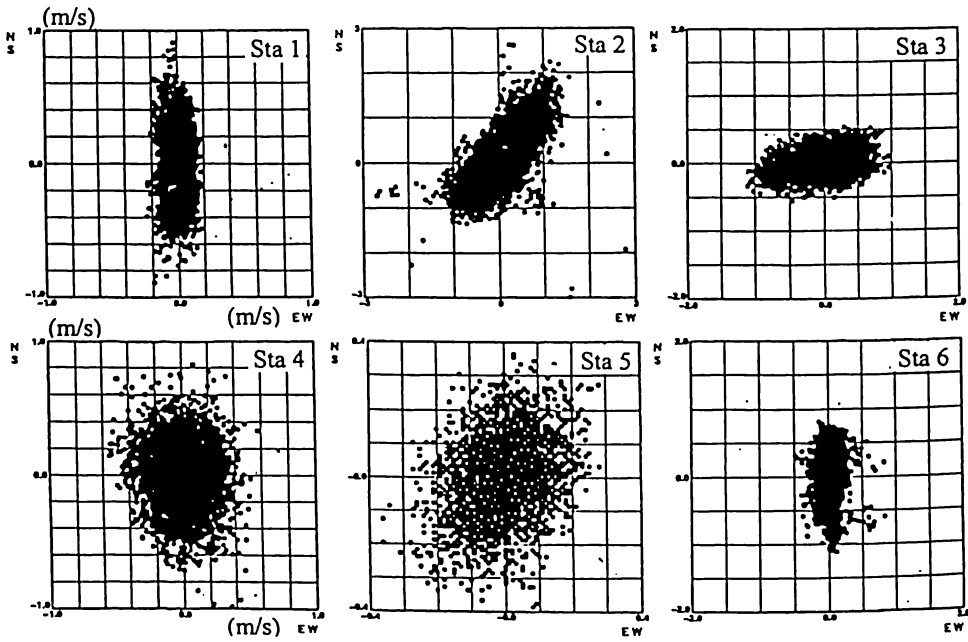
Figure 12. Measured horizontal velocities, Case 97.03.30.06
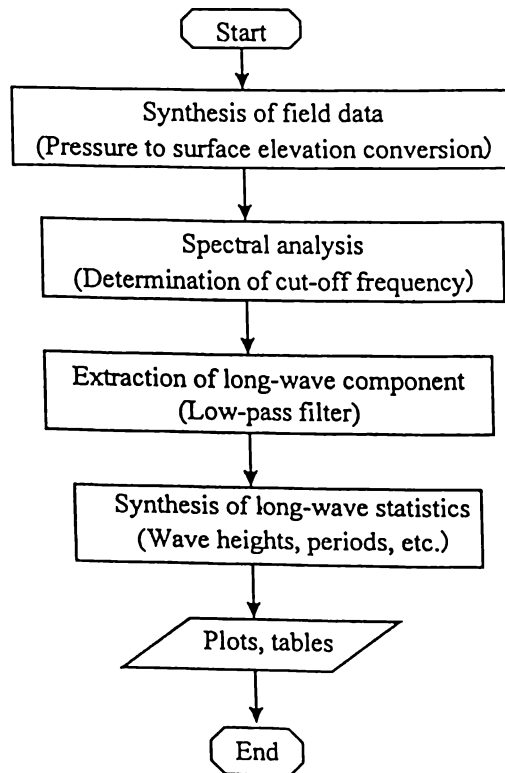
Figure 13. Flowchart for synthesis of long period oscillations
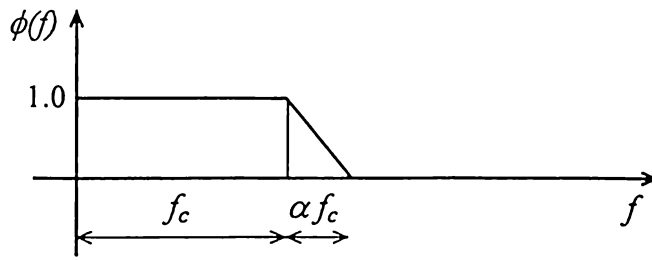
Figure 14. Filter function for extraction of long period oscillations
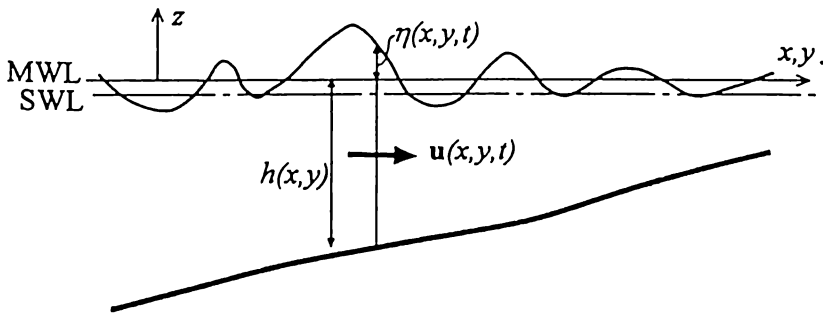
Figure 15. Definition of variables
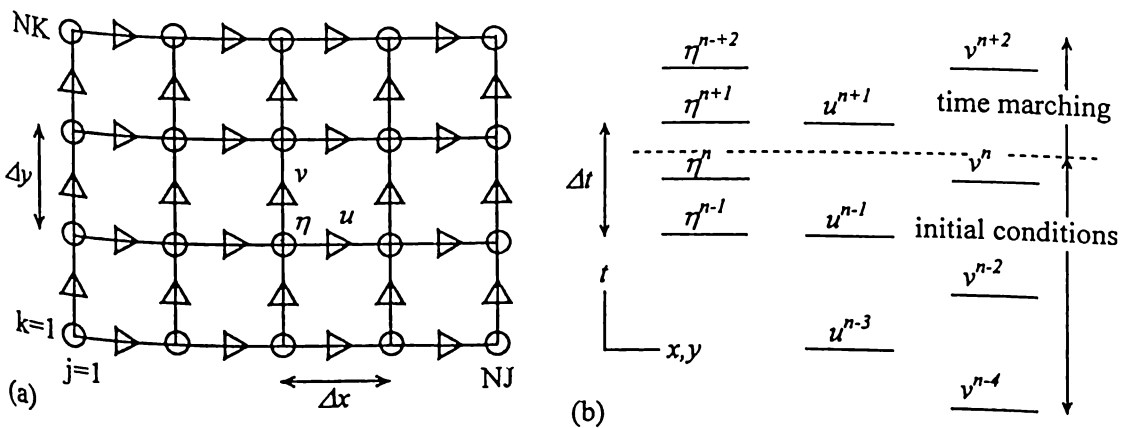
Figure 16. Numerical implementation. (a) Finite difference grid (b) Time-splitting method

45
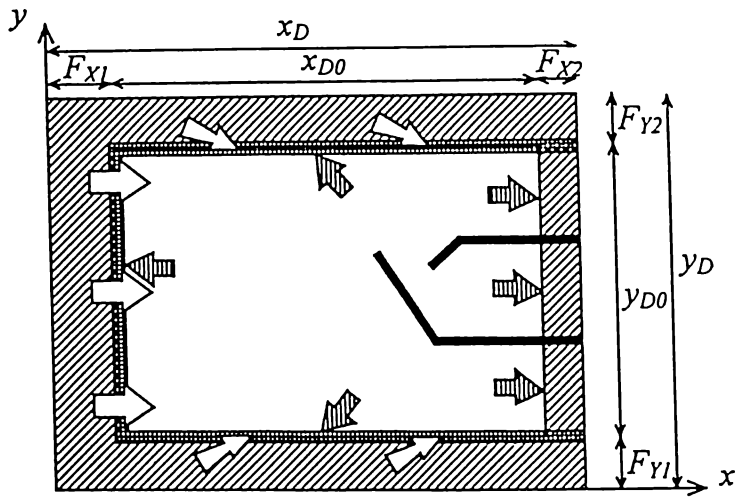
	Region	Description
	coexistence	Progressive wave + reflected wave + scattered waves
	boundary damping	outgoing waves only
	incidence zone	prescribed incident wave

	Wave type
	incident wave
	outgoing wave
	side incident wave

Figure 17. Zones of computation region
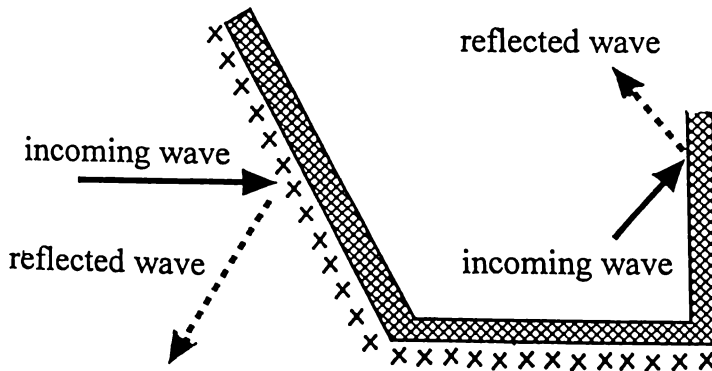
Figure 18. Reflection at structure interfaces
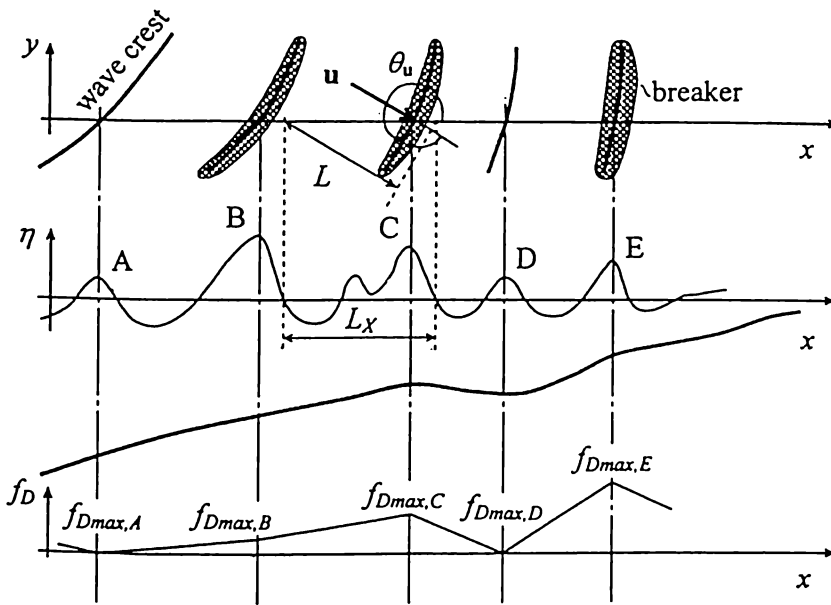
Figure 19. Parameters of wave breaking model
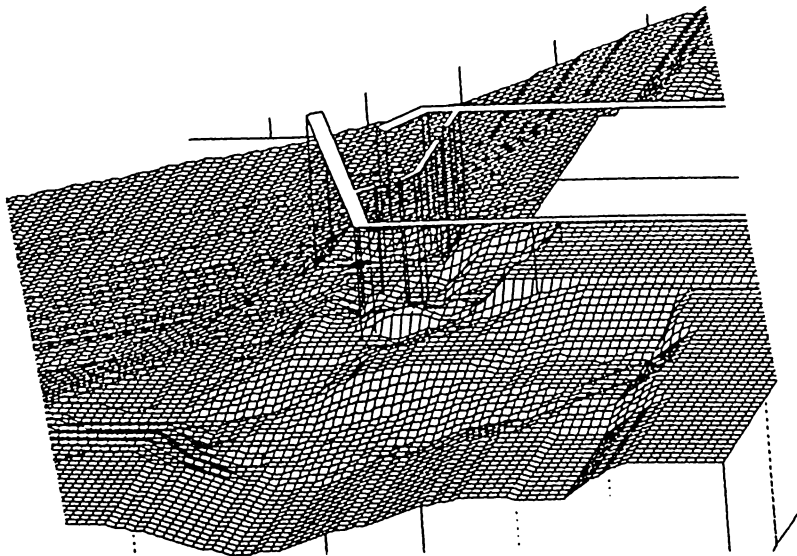
Figure 20. Discretized bathymetry (interior depths based on data taken December 1995)

47
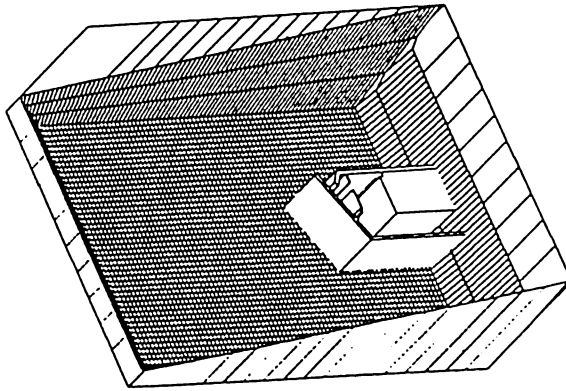
Figure 21. Boundary damping distribution
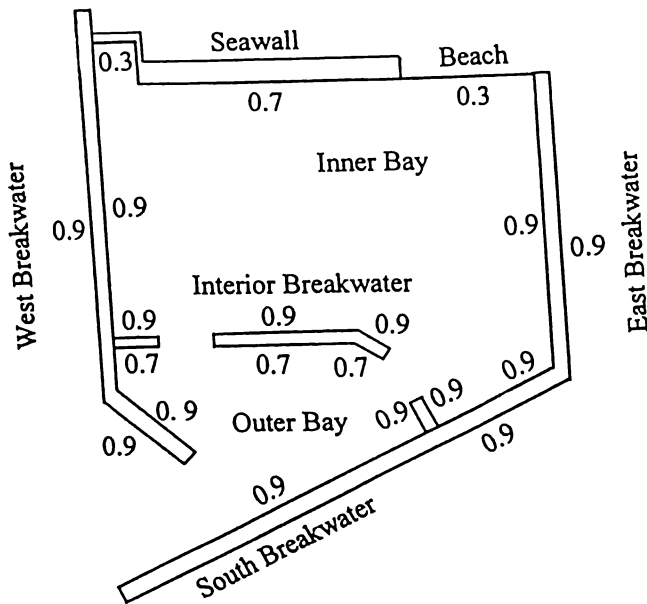
Figure 22. Reflection coefficients used in the computations

48

97.03.30.06   h=19.26+1.21m
Sign.Wave: H=2.62m T=8.3s   Measured   Computed
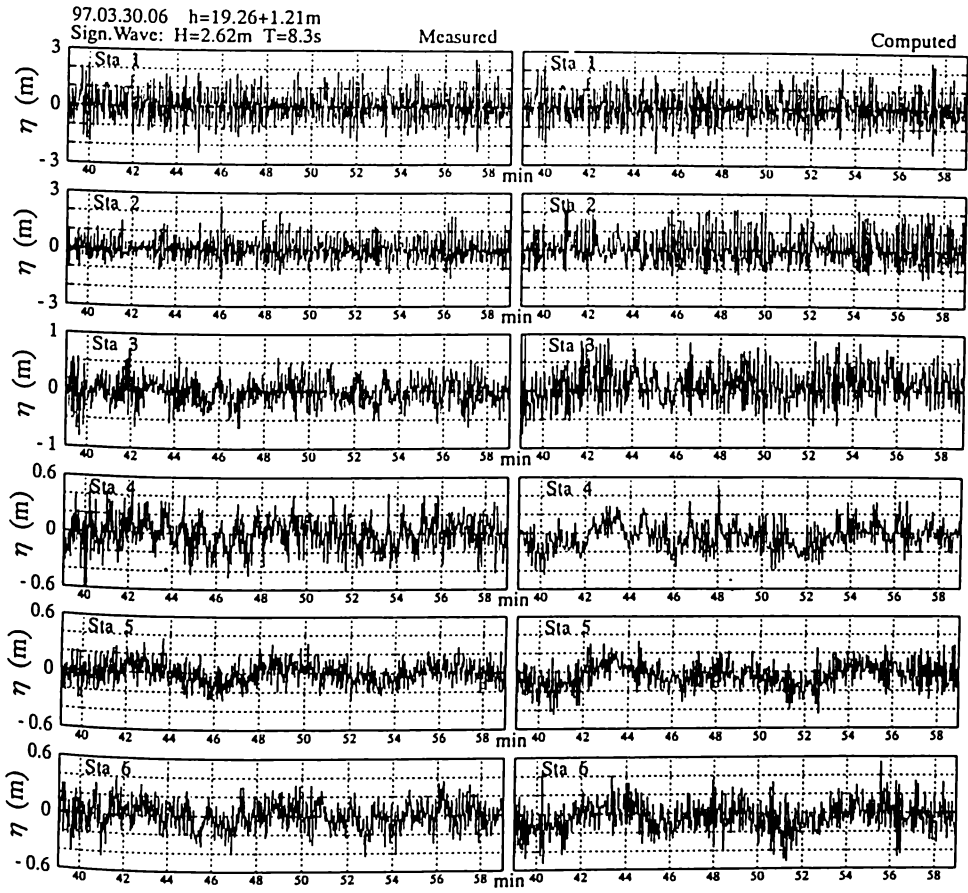
Figure 23. Measured and computed time series $\eta(t)$ at Stations 1 to 6, Case A
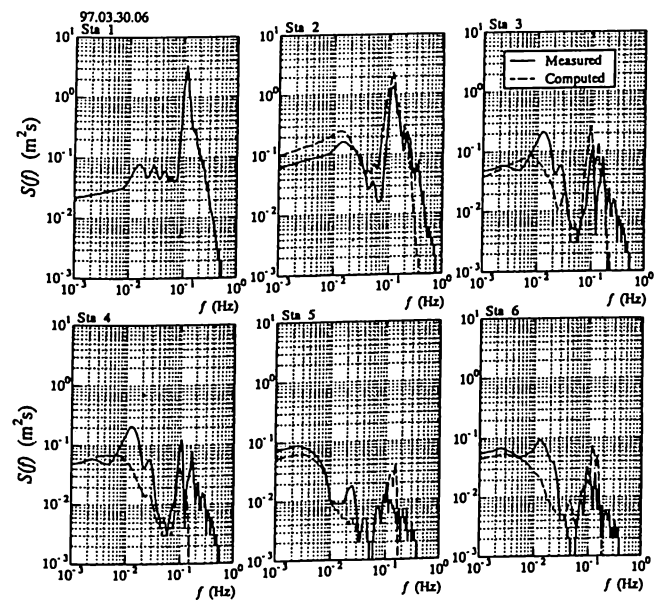
Figure 24. Frequency spectra of measured and computed $\eta(t)$ at Stations 1 to 6, Case A

49

97.04.23.14   h=19.26+0.70m
Sign.Wave: H=1.57m   T=13.2s   Measured   Computed
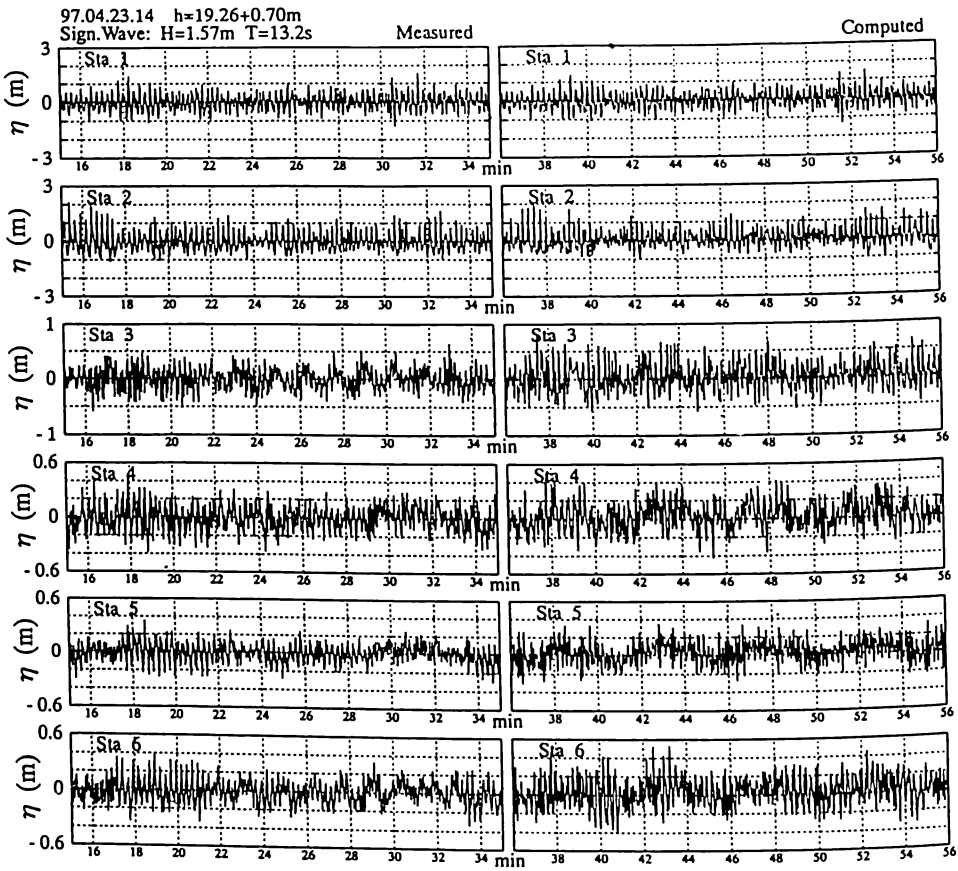
Figure 25. Measured and computed time series $\eta(t)$ at Stations 1 to 6, Case B
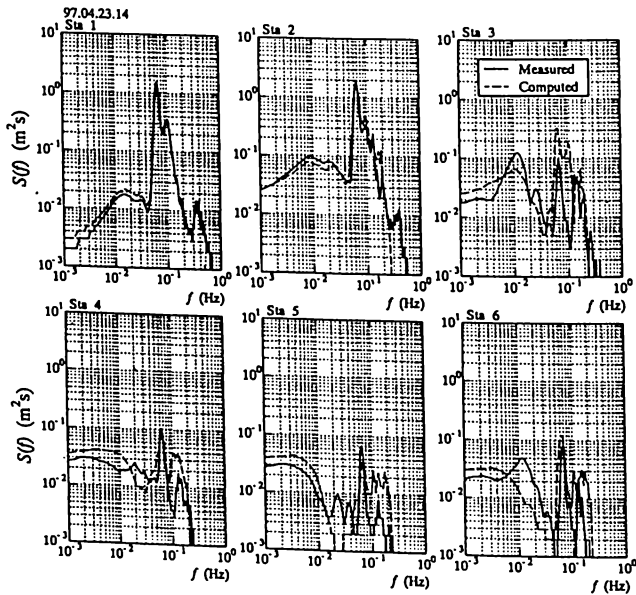
Figure 26. Frequency spectra of measured and computed $\eta(t)$ at Stations 1 to 6, Case B

50
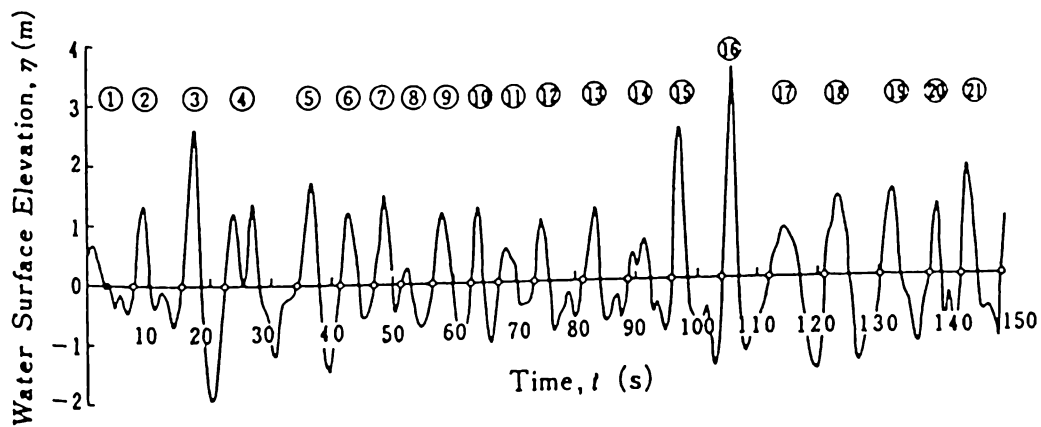
Figure 27. Individual wave analysis by zero-up-crossing method (From Goda, 1985)
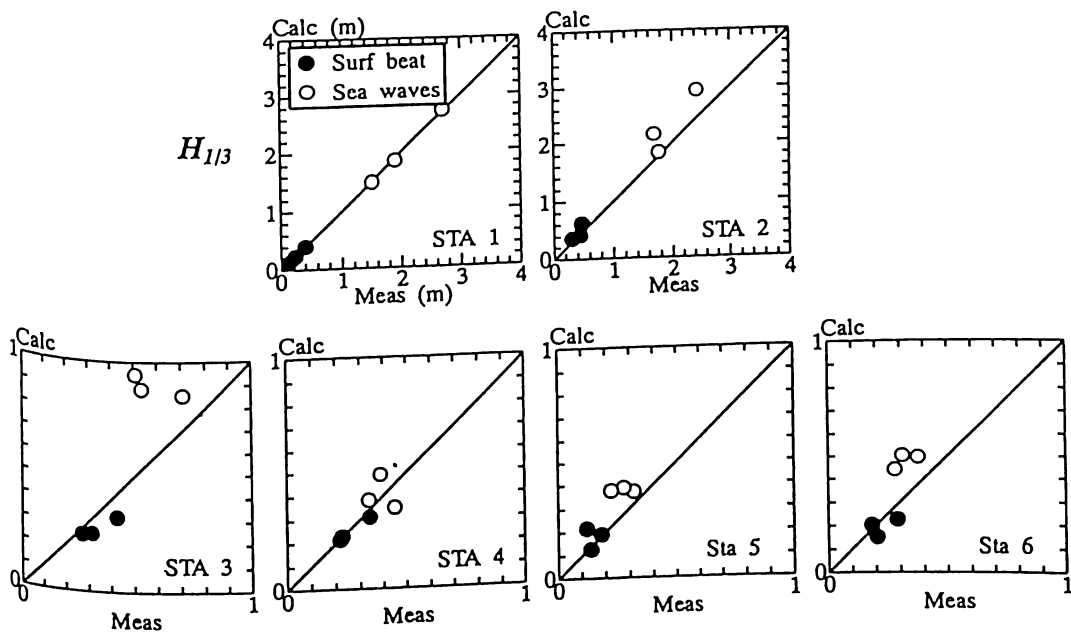
Figure 28. Comparison of measured and computed $H_{1/3}$ for long period oscillations (surf beat) and sea waves
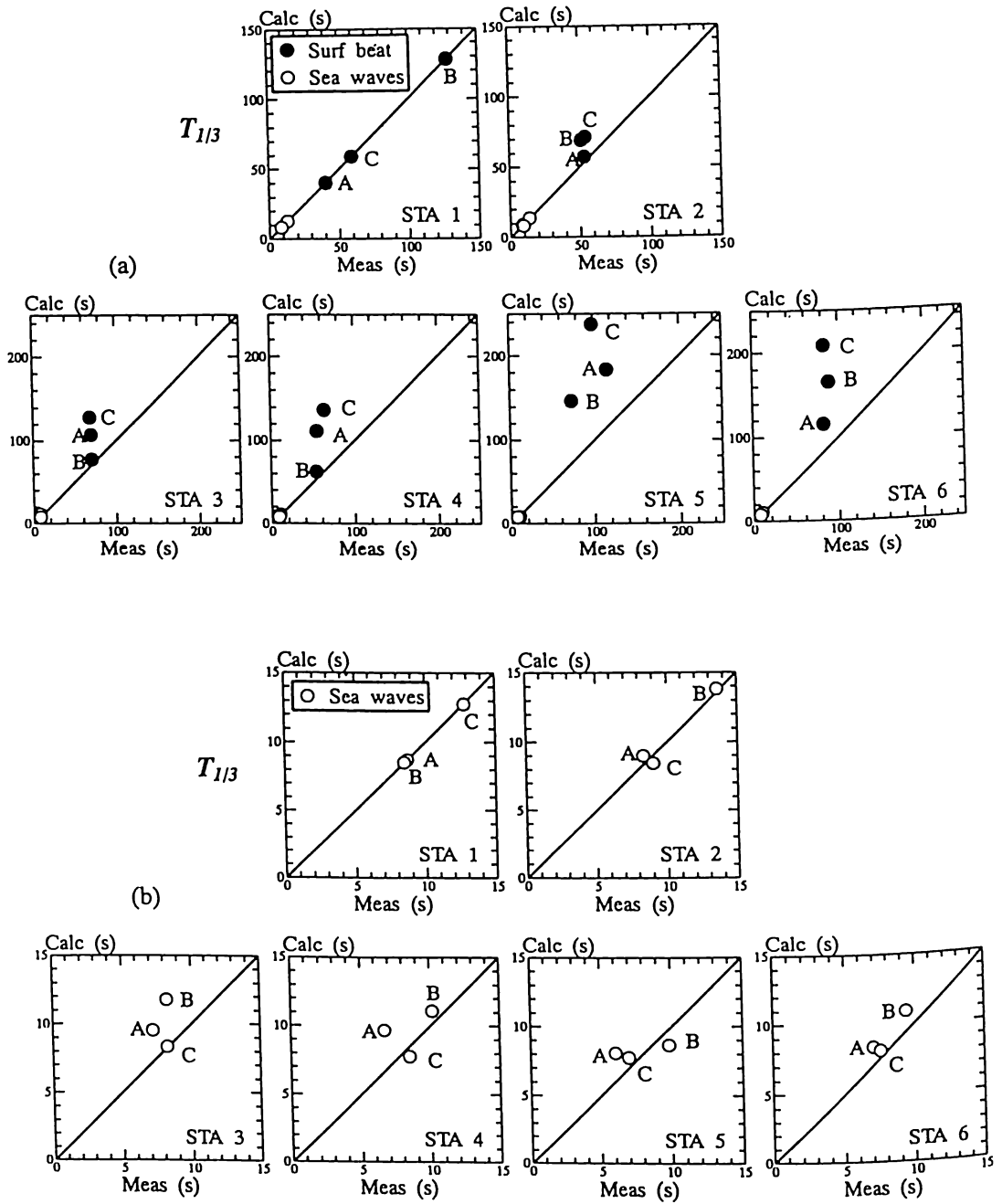
Figure 29. Comparison of measured and computed $T_{1/3}$ for (a) long period oscillations and (b) sea waves

52
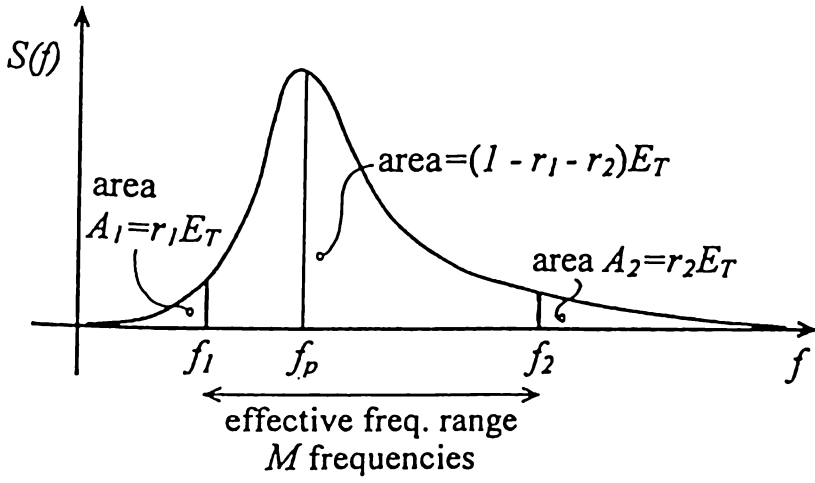
Figure 30. Parameters of frequency spectrum
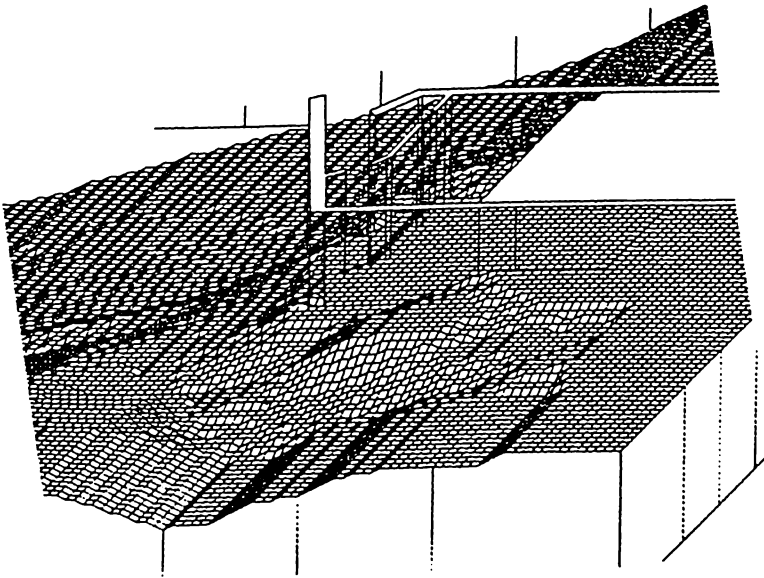
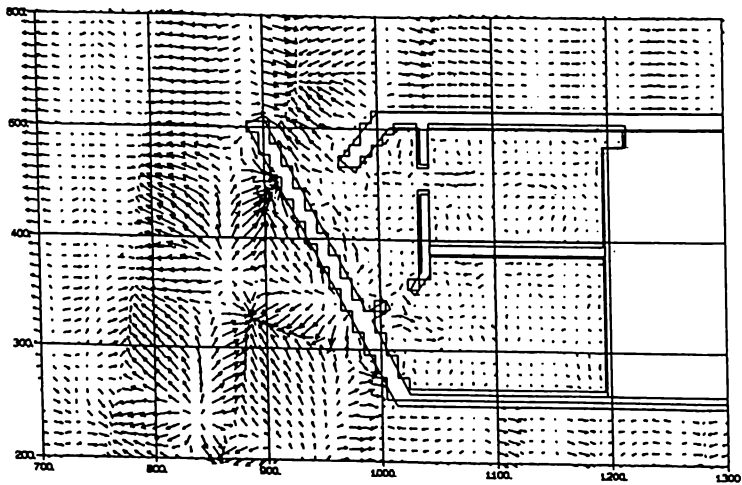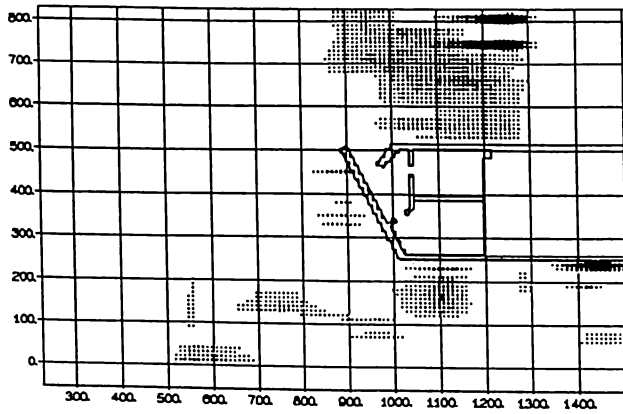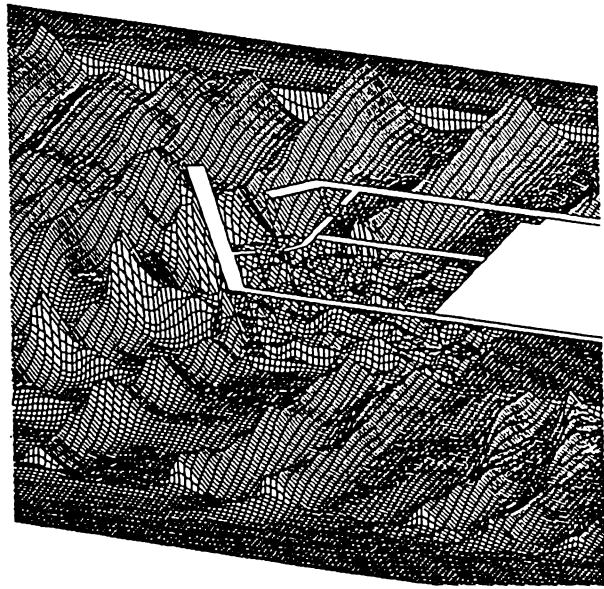**Figure 31.** Bathymetry and structure configuration, nonpartitioned inner bay
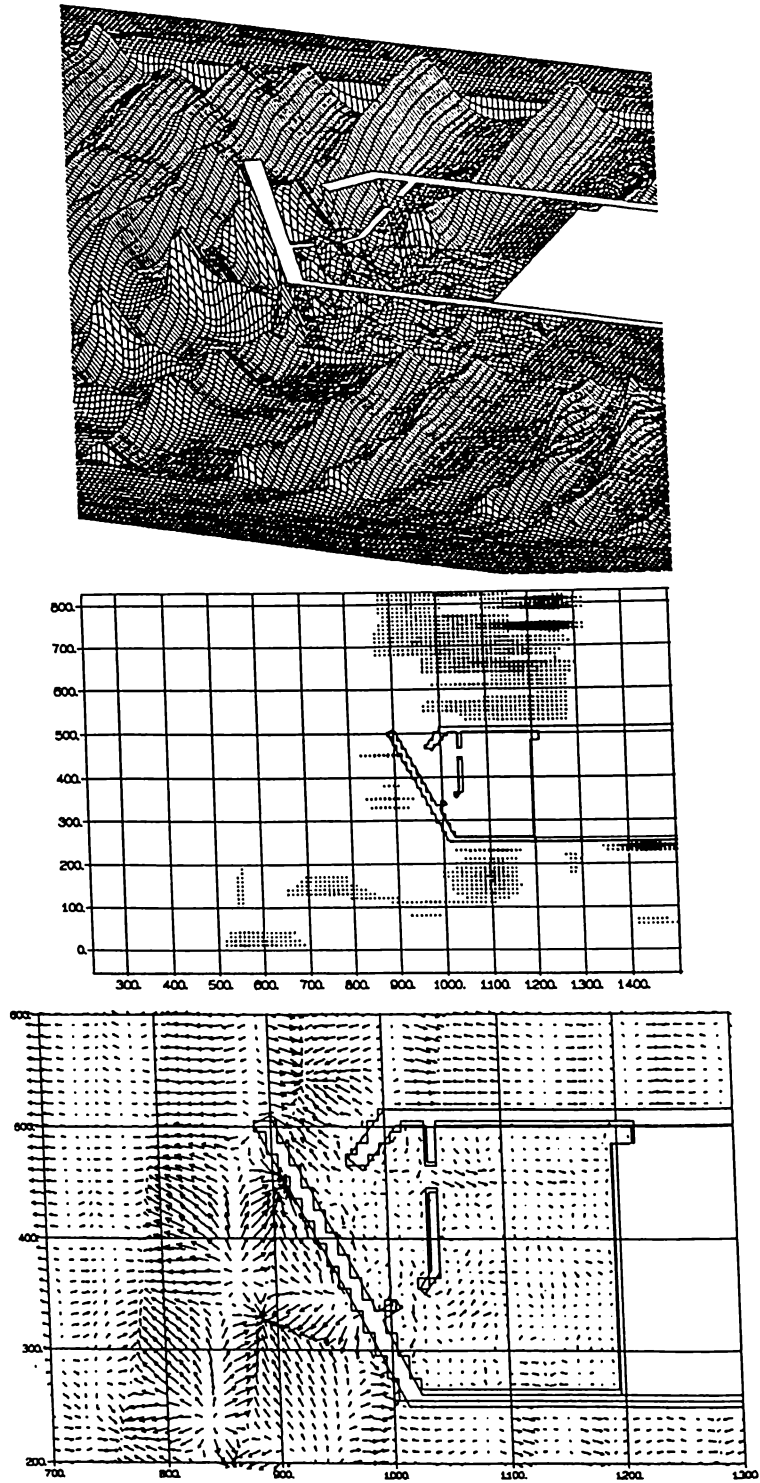
Figure 32. Transient wave field due to design wave, nonpartitioned inner bay. (a) $\eta(x,y,t)$ (b) Breaking dissipation zones $f(x,y,t)$ (c) $u(x,y,t)$
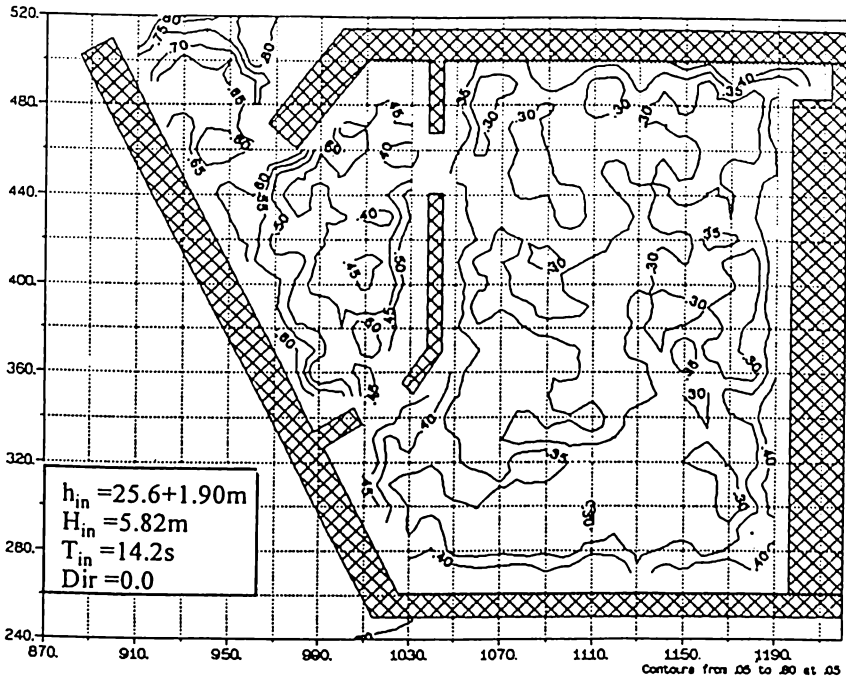
Figure 33. Contours of maximum wave height (normalized by H_{in}), nonpartitioned inner bay, due to design wave
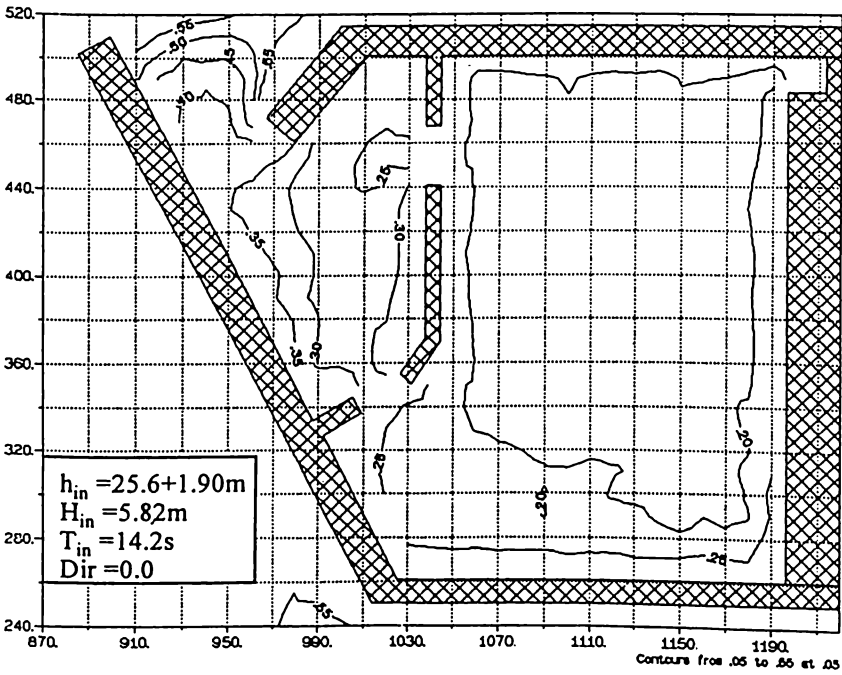
Figure 34. Contours of significant wave height (normalized by H_{in}), nonpartitioned inner bay, due to design wave

55

Figure 35. Transient wave field due to design wave, partitioned inner bay. (a) $\eta(x,y,t)$ (b) Breaking dissipation zones $f_D(x,y,t)$ (c) $u(x,y,t)$
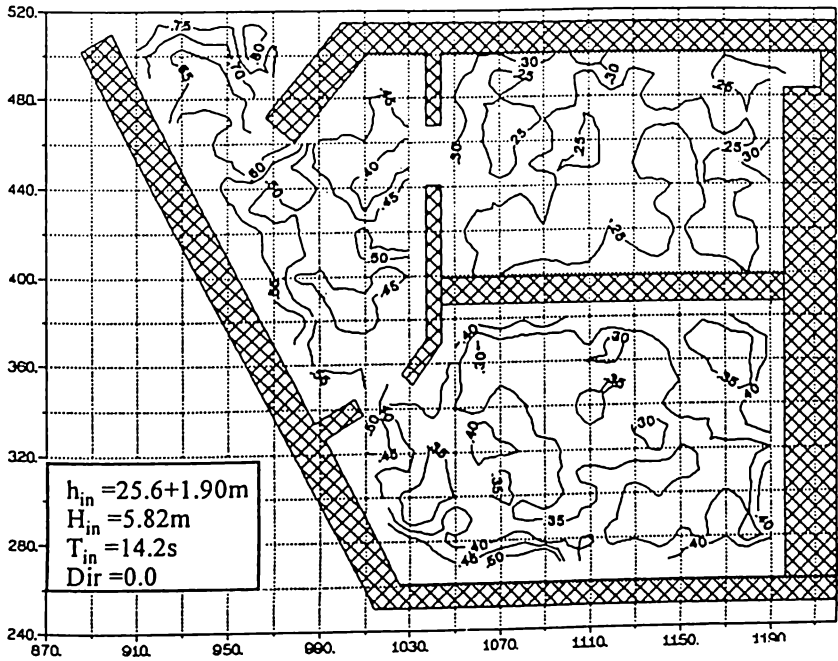
56

Figure 36. Contours of maximum wave height (normalized by H_{in}), partitioned inner bay, due to design wave
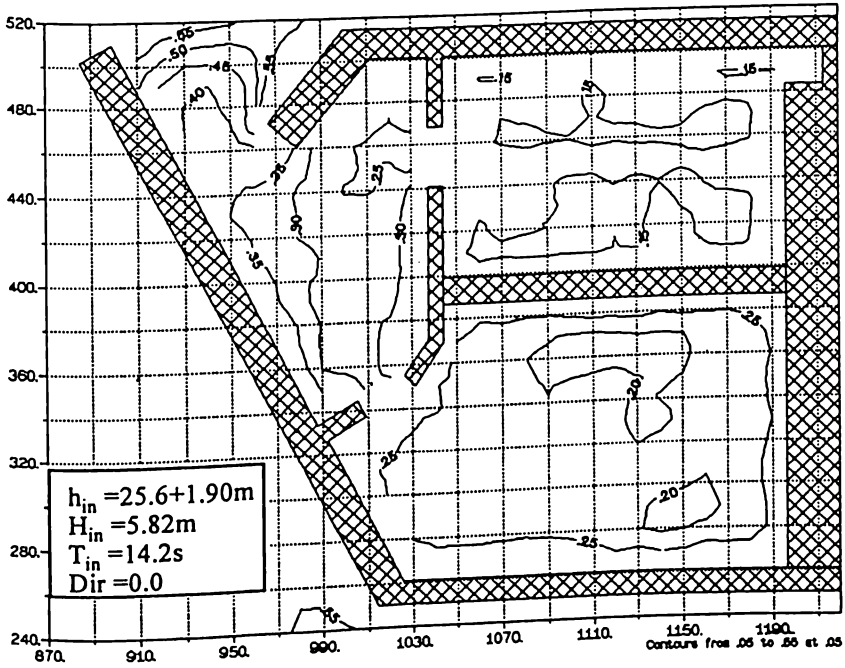

Figure 37. Contours of significant wave height (normalized by H_{in}), partitioned inner bay, due to design wave

57